BRNO UNIVERSITY OF TECHNOLOGY

Faculty of Electrical Engineering
and Communication

BACHELOR'S THESIS

Brno, 2018 Jan Svatoň

BRNO UNIVERSITY OF TECHNOLOGY
VYSOKÉ UČENÍ TECHNICKÉ V BRNĚ

FACULTY OF ELECTRICAL ENGINEERING AND COMMUNICATION
FAKULTA ELEKTROTECHNIKY
A KOMUNIKAČNÍCH TECHNOLOGIÍ

DEPARTMENT OF BIOMEDICAL ENGINEERING
ÚSTAV BIOMEDICÍNSKÉHO INŽENÝRSTVÍ

REDUCTION OF MOVEMENT ARTIFACTS IN BOLD FMRI DATA USING REJECTION OF MOTION-CORRUPTED SCANS

REDUKCE POHYBOVÝCH ARTEFAKTŮ V DATECH BOLD FMRI S VYUŽITÍM ELIMINACE VLIVU POHYBEM

BACHELOR'S THESIS
BAKALÁŘSKÁ PRÁCE

AUTHOR
AUTOR PRÁCE
Jan Svatoň

SUPERVISOR
VEDOUCÍ PRÁCE
Ing. Michal Mikl, Ph.D.

BRNO 2018

BRNO UNIVERSITY OF TECHNOLOGY
FACULTY OF ELECTRICAL ENGINEERING AND COMMUNICATION

Bachelor's Thesis

Bachelor's study field **Biomedical Technology and Bioinformatics**
Department of Biomedical Engineering

Student: Jan Svatoň ***ID:*** 186692
Year of study: 3 ***Academic year:*** 2017/18

TITLE OF THESIS:

Reduction of movement artifacts in BOLD fMRI data using rejection of motion-corrupted scans

INSTRUCTION:

1) Carry out a literary review of magnetic resonance imaging (fMRI) methods with regard to the expressions of movement artifacts and methods of detection and suppression of these artifacts. 2) Choose at least two suitable methods for locating affected scans in the BOLD fMRI data. 3) Next, suggest ways to eliminate the impact of these scans. 4) Implement the proposed methods from points 2 and 3 in the MATLAB software. 5) In cooperation with the Multimodal and Functional Imaging Laboratory of CEITEC MU, test the functionality of the created software and compare the various variants of the artifact removal procedure (i.e. compare the effect of removing affected scans on the results of the fMRI data analysis) on a suitable dataset. 6) Evaluate the obtained results and recommend a suitable way of eliminating movement artifacts in the data.

RECOMMENDED LITERATURE:

[1] Power, J.D., Barnes, K.A., Snyder, A.Z., Schlaggar, B.L., Petersen, S.E., 2012. Spurious but systematic correlations in functional connectivity MRI networks arise from subject motion. NeuroImage 59, 2142–2154.

[2] Power, J.D., Mitra, A., Laumann, T.O., Snyder, A.Z., Schlaggar, B.L., Petersen, S.E., 2014. Methods to detect, characterize, and remove motion artifact in resting state fMRI. NeuroImage 84, 320–341.

Date of project specification: 5.2.2018 ***Deadline for submission:*** 25.5.2018

Leader: Ing. Michal Mikl, Ph.D.
Consultant:

prof. Ing. Ivo Provazník, Ph.D.
Subject Council chairman

ABSTRACT

This bachelor thesis first deals with the elementary principles of function magnetic resonance and the sources of noise and artifacts in the data. Furthermore, the thesis elaborates on the motion artifact phenomena and suggests two suitable methods for locating and eliminating motion-affected scans in the BOLD fMRI data. The methods are then implemented in the MATLAB environment and tested on suitable datasets provided by the Multimodal and Functional Imaging Laboratory of CEITEC MU. Finally, the results are presented and evaluated along with a recommendation for a suitable way of eliminating movement artifacts in the data.

KEYWORDS

Motion artifact, motion scrubbing, spike regression, BOLD fMRI, General Linear Model

ABSTRAKT

Tato bakalářská práce ze zprvu zabývá elementárními principy magnetické rezonance a zdrojů šumu a artefaktů v datech. Dále práce podrobněji pojednává o pohybovém artefaktu a navrhuje dvě vhodné metody pro lokalizaci a odstranění pohybem postižených skenů BOLD fMRI dat. Metody jsou poté implementovány v prostředí MATLAB a otestovány na vhodných datasetech poskytnutých Laboratoří multimodálního a funkčního zobrazování, CEITEC MU. Nakonec jsou prezentovány a vyhodnoceny výsledky zároveň s doporučením pro vhodný způsob eliminace pohybového artefaktu v datech.

KLÍČOVÁ SLOVA

Pohybový artefakt, motion scrubbing, spike regression, BOLD fMRI, Obecný lineární model

SVATOŇ, Jan. *Reduction of movement artifacts in BOLD fMRI data using rejection of motion-corrupted scans*. Brno, 2018, 76 p. Bachelor's Thesis. Brno University of Technology, Faculty of Electrical Engineering and Communication, Department of Biomedical Engineering. Advised by Ing. Michal Mikl, Ph.D.

DECLARATION

I declare that I have written the Bachelor's Thesis titled "Reduction of movement artifacts in BOLD fMRI data using rejection of motion-corrupted scans" independently, under the guidance of the advisor and using exclusively the technical references and other sources of information cited in the thesis and listed in the comprehensive bibliography at the end of the thesis.

As the author I furthermore declare that, with respect to the creation of this Bachelor's Thesis, I have not infringed any copyright or violated anyone's personal and/or ownership rights. In this context, I am fully aware of the consequences of breaking Regulation § 11 of the Copyright Act No. 121/2000 Coll. of the Czech Republic, as amended, and of any breach of rights related to intellectual property or introduced within amendments to relevant Acts such as the Intellectual Property Act or the Criminal Code, Act No. 40/2009 Coll., Section 2, Head VI, Part 4.

Brno ....

author's signature

ACKNOWLEDGEMENT

I would like to thank my supervisor, Ing. Michal Mikl, Ph.D. and my consultant, Ing. Marie Nováková. Without their assistance and dedicated involvement in every step throughout the process, this thesis would have never been accomplished. Finally, let me thank to my dear friend, Cynthia Miles, who devotedly proofread the thesis. I would like to thank you all very much for your support, kindness and patience.

Brno . . . .

author's signature

CONTENTS

LIST OF FIGURES

LIST OF TABLES

INTRODUCTION

Today functional magnetic resonance imaging or functional MRI (fMRI) is one of the leading methods in both neuroscience research and psychiatric practice. To obtain sharp images that can be reliably used for further statistical analyzes, it is crucial for the subject to restrain any movements and thus avoid devastating motion artifacts. This can especially be a problem for children or people with Parkinson's disease. However, even healthy adults do move due to breathing or the nature of the fMRI study itself.

To overcome this problem, most laboratories use head restraints of some form, such as bite bars, masks, vacuum packs, padding, or taping. Unfortunately they do not eliminate the motion artifact completely.

There are several ways how to cope with the motion artifact in the preprocessing of the fMRI data: either use motion regressors (that do not remove the artifact completely), or perform motion scrubbing of the data, or construct special regressors that would except motion-affected scans from further analyzes.

The comparison of such techniques is the objective of this thesis, along with their implementation into a MATLAB-based application. The objective is particularly interesting, since very few studies, if any, have produced such a wide and thorough comparison using fMRI data acquired with different field strength intensities.

The theoretical part of the thesis first covers a comparison of fMRI with different functional imaging techniques and then further elaborates on the basic physical principals underlying fMRI, explains how an fMRI image is produced, what artifacts deteriorate the image quality and what preprocessing steps need to be taken. At the end of the theoretical part there is a basic explanation of the General Linear Model and, most importantly, a description of detecting methods of motion-affected scans, along with their removal and substitution techniques.

The applied part of the thesis suggests two suitable methods for locating and eliminating motion-affected scans in the BOLD fMRI data. The methods are then implemented in MATLAB environment and tested on suitable datasets provided by the Multimodal and Functional Imaging Laboratory of CEITEC MU. In the end the results are presented and evaluated along with a recommendation for suitable way of eliminating movement artifacts in the data.

1 FMRI IN RESPECT TO OTHER FUNCTIONAL IMAGING TECHNIQUES

Functional magnetic resonance imaging (fMRI) is undoubtedly the leading method in neuroscience with tens of thousands of experiments based on this imaging technique. FMRI along with PET, EEG and MEG comprise the four most used functional neuroimaging methods in clinical practice. Such methods are employed to acquire bioelectrical signals of neural activity. However, they differ not only in their underlying physical principals and spatial and temporal resolutions, but also in the nature of the image we want to acquire. Thus each method is suitable for different types of tasks and has its pros and cons [7] [11].

The oldest of the above-mentioned methods is EEG (Electroencephalography). The first application of EEG dates back to 1877 when Richard Caton acquired the very first recording of electrical activity from exposed brains of rabbits and monkeys using a mirror galvanometer. It was not until 1924 that Hans Berger successfully measured electrical activity in the human brain and paved the way for the upcoming golden era of the EEG that began in the 1960's [4] [11] [13].

EEG records electrical activity of the brain through electrodes attached to the scalp. Another similar technique is MEG (Magnetoencephalography) which was introduced later in the mid 1980's due to its arduous technological complexity. MEG stems from the same physiological phenomena as EEG: it non-invasively measures post-synaptic potentials between cortical neurons by the means of induced magnetic signals. Note that the generation of the signal is often erroneously contributed to ionic currents of propagating action potentials. Since in both methods the acquired signal is a sum from a larger volume of cortex and is dulled by the skull and cerebrospinal fluid. The resulting spatial resolution is relatively poor, identifying the approximate location of activity to within about a centimeter. On the other hand, the temporal resolution is very high, showing changes within milliseconds. While MEG achieves better results than EEG in spatial resolution, this benefit must be considered against the complexity and fragility of the MEG machine, along with its costs [11] [13].

PET (Positron-emission tomography) emerged later, in the mid 1970's. PET is based on using radioactive tracers (radiopharmaceuticals) to observe and trace the metabolic processes and paths in the body. The choice of radioactive tracers depends upon the metabolic processes we want to follow. In the functional imaging of the brain, the most used tracer is Fluorine-18 (F-18) Fluorodeoxyglucose (FDG), which is essentially a radioactive isotope of glucose. This can be explained by the brain's

need for glucose, since it is the only source of energy that crosses the blood–brain barrier [1] [11].

The underlying physical principal of PET lies in positron emission (also known as β^+ decay). As the radioactive tracer decays it emits a positron, which then travels a distance up to one millimeter and collides with an electron. During this collision the positron and the electron (antiparticles) are annihilated and give rise to two photons that radiate in exactly opposite directions. Only thanks to this phenomenon can we localize the source of the radiation: by putting a patient inside a ring-shaped detector and detecting only those photons that were registered both simultaneously and in approximately opposite directions [1] [11].

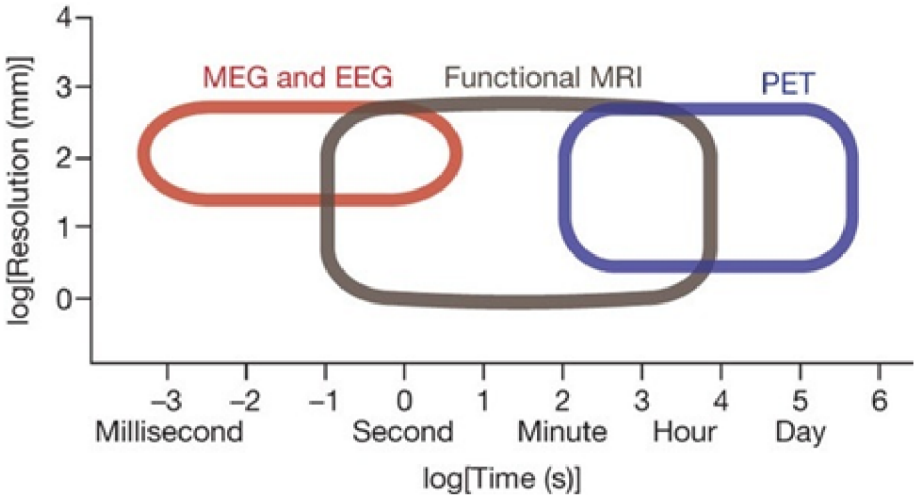

Fig. 1.1: Comparison of various functional imaging techniques [13]

2 BASIC PRINCIPLES OF (F)MRI

In this chapter I am going to explain the basic principles of (f)MRI. In the text the terms fMRI and MRI may be interchanged, since they both are based on the same principles.

2.1 Nuclear Magnetism

MRI images are usually acquired using hydrogen nuclei that are abundant in the human body. However, other isotopes such as ^{3}He, ^{23}Na or ^{31}P are also possible sources. All those isotopes share the same quantum mechanical feature: a non-zero spin. In other words, the nuclei do not have the same number of protons and neutrons and, therefore, can be utilized in the nuclear magnetic resonance process. This magnetic imbalance of elements is referred to as the magnetic dipole moment and denoted as μ. To quantify the vector of the magnetic moment, imagine a positively charged nucleus (e.g. hydrogen) rotating on its axis. This rotation (or spinning) is caused by thermal energy. The magnetic dipole moment can then be defined by the right-hand rule as following [7] [10]

$$\mu = I * A \tag{2.1}$$

with I being a tiny current traveling around the edge of a cross sectional area (A).

The next parameter of these nuclei that is worth noting is the gyromagnetic ratio (γ). The gyromagnetic ratio is a ratio between the charge and the mass of a spinning nucleus. Since only stable nuclei are used in MRI, the gyromagnetic ratio represents a unique constant for each isotope.[7]

$$\gamma = \frac{q}{2m} \tag{2.2}$$

2.2 Spins within Magnetic Fields

When there are a number of spinning nuclei with magnetic dipole moment, they orient themselves randomly and thus have no net magnetization. However, after a strong external magnetic field B_0 is applied, nuclei try to reach the equilibrium state either by assuming parallel or antiparallel orientation with the vector of the external magnetic field. The parallel state has lower energy and is more stable than the antiparallel state and is, therefore, more frequent. This leads to the total net magnetization M_z of the nuclei as shown in Figure 2.1 [7] [10].

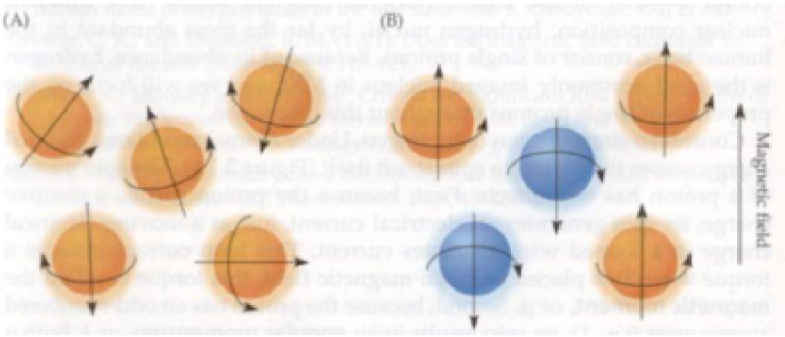

Fig. 2.1: Ilustration of applying an external magnetic field to randomly orientated nuclei. Net magnetization vector M_z points in the same direction as the vector of the external magnetic field B_0 [7]

2.3 Precession and Larmour Frequency

Atomic nuclei in the low-energy state (parallel) can be tilted to the high-energy state (antiparallel) by providing the nuclei with energy that is equal to the difference of the energy between the two states. Conversely, nuclei in the high-energy state can radiate this energy and assume the low-energy state. This shifting energy can be supplied in the form of an electromagnetic pulse, whose frequency is described by the Bohr relation [7] [10]

$$f = \frac{\Delta E}{h} \tag{2.3}$$

where h is the Planck constant. The equation can be rewritten after substituting energy E with equations describing the total supplied work as [7]

$$f = \frac{\gamma}{2\pi} B_0 \tag{2.4}$$

This frequency is referred to as the **Larmor frequency**. By looking at the equation we can see that the frequency is defined only by the gyromagnetic ratio (equation 2.2) and the applied external magnetic field B_0 (usually 1.5T or 3.0T). Since the gyromagnetic ratio is unique for every atomic nuclei, so must be the Larmor frequency. Therefore, we can easily aim at different nuclei and change their energy states [7] [10].

In Figure 2.1 we have seen how applying an external magnetic field to atoms makes up a net magnetization. In reality, however, the nuclei are not perfectly aligned with the axis of the magnetic field. Instead, in addition to their intrinsic spins, atoms perform rotational movements about this axis. This rotational movement, depicted

in Figure 2.2, is known as **precession**. Remarkably, the angular frequency of precession is the same as the Larmor frequency of a given nucleus. This correspondence is crucial for the MR signal generation [7] [10].

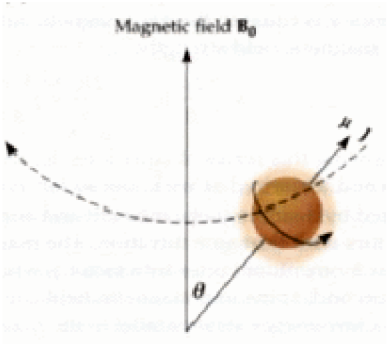

Fig. 2.2: Illustration of precession and intrinsic rotation of a nucleus about Z axis [7]

2.4 Application of a Radiofrequency Pulse

Application of an excitational radiofrequency pulse (RF pulse) of Larmor frequency of a given nuclei to a sample from a lateral direction (XY plane) leads to two processes: (1) half of the nuclei switches from the parallel to the antiparallel state and (2) all spins synchronize to the same phase. As s consequence, the net magnetization M_z begins to fade away to be increased in the XY plane as M_{xy} (see Figure 2.3). This phenomenon, where small applications of energy at a particular frequency induce larger changes in the system, is referred to as resonance [7] [10].

Depending on the length we transmit the RF pulse, we can tilt the atoms to various angles Θ:

$$\Theta(t) = \gamma * \int_{t'=0}^{t} B_1(t')dt' \tag{2.5}$$

These angles are known as flipping angles, of which the most frequently used are 90° and 180° angles. Note that by applying 90° RF pulse, the longitudinal magnetization M_z diminishes to maximize the transverse magnetization M_{xy} and thus amplify the whole signal (since we receive the MR signal in the transverse plane, the growth of M_{xy} naturally leads to greater amplitude of the signal). Conversely, after applying 180° RF pulse, vector M_{xy} diminishes to maximize M_z and there is no detectable signal [7] [10].

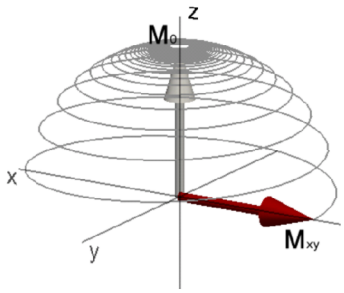

Fig. 2.3: Spiraling change (i.e. nutation) of a net magnetization after a 90° radiofrequency pulse caused by diminishing M_z magnetization and growth of M_{xy} magnetization [8]

2.5 Spin Relaxation

When the radiofrequency pulse is taken away, the system starts returning to its equilibrium state by radiating energy. This process is referred to as spin relaxation, which causes the loss of the MR signal. The relaxation can be longitudinal or transverse [7] [10].

Longitudinal relaxation is characterized by the loss of energy we provided the system by an RF pulse. The energy is radiated by spins going from the high-energy (antiparallel) states to their original low-energy (parallel) states. This leads to re-arising M_z magnetization, as there was before the RF pulse (Figure 2.3). The time at which 63 % of atoms return to their original parallel state is referred to as T_1 [7] [10].

Transverse relaxation starts much earlier, long before longitudinal relaxation is finished. The so-far coherent spins begin to dephase and as a result the net transverse magnetization M_{xy} begins to diminish. There are two causes of the dephasing process: intrinsic and extrinsic.

Intrinsic dephasing stems from the interactions between two spins: one altering the angular velocity of the other (known as T_2 decay). T_2 is then the time for the transverse magnetization M_{xy} to fall to 37 % of its initial value.

Extrinsic dephasing, on the other hand, arises from inhomogenities in the external magnetic field, changing the precessing frequency (see equation 2.2), which in turn leads to dephasing. The combination of both types of dephasing is referred to as T_2^* decay, which is essential for BOLD fMRI [7] [10].

T_1 and T_2 decay times are specific for each type of tissue and thus they enable us to magnify the contrast of the tissue we are interested in with regard to surrounding tissues. This process in known as T_1 or T_2 weighting, which is accomplished by

Tab. 2.1: Rough Values of T_1 and T_2 Times at a Field Strength of 1.5 T

	Gray Matter	White Matter	Cerebrospinal Fluid
T1	900 ms	600 ms	4000 ms
T2	100 ms	80 ms	2000 ms

changing the time at which the RF pulse is repeated (repetition time (TR)) or the time at which the image is acquired (echo time (TE)), respectively [7] [10].

2.6 Image Acquisition

As the net magnetization vector is rotating in the XY plane, it creates magnetic waves which are then detected in receiving coils in the form of a magnetic flux. Magnetic flux, governed by Faraday's law of induction, then in return creates a current and provides a readable signal (see Figure 2.4) [7].

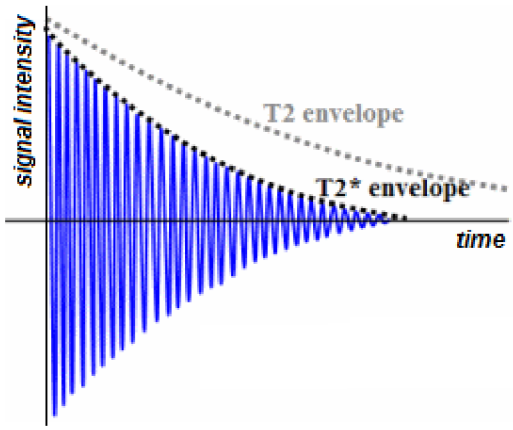

Fig. 2.4: Illustration of T_2 and T_2* decay after applying a radiofrequency pulse, also known as free induction decay(FID) [6]

2.7 Slice Selection

We now know how the signal from our object (e.g. brain) is obtained. However, how can we focus on a specific slice and not on the whole object? We can infer from the equation 2.2 that magnetic gradients, instead of a uniform magnetization throughout the sample, could be a solution: each nucleus would then have the unique properties of a Larmor frequency and a phase.

To obtain a 2D image from a 3D sample, we need in total 3 gradients that will govern coding in all directions X, Y and Z. Those 3 gradients are known as G_f, G_ϕ and G_{sl}, respectively. The slice-selection encoding gradient G_{sl} enables us to select a specific slice within the sample. After applying a radiofrequency pulse of a frequency to the slice we want to select, only the nuclei in this slice would be excited and, therefore, contribute to the image formation. This process breaks down the problem to a 2D space.

Shortly after turning on the G_{sl} and a RF pulse, the phase-encoding gradient G_ϕ is applied. This gradient G_ϕ ensures that spins accumulate different phase offsets over space.

At last the frequency-encoding gradient G_f is applied at the same time as we turn on the receiving coils and detect the signal. Hence, the spin precession frequency changes over space [7] [10].

Ultimately we are alternating the phase-encoding gradient G_ϕ and frequency-encoding gradient G_f, scanning the slice of the object line by line from one side to the other. In fMRI imaging this technique is referred to as gradient echo (gradient echo (GRE)) imaging [7] [10].

2.8 K-space and Resolution of The Image

The signal we obtain is not of the final image itself, but it is a representation of the image in a spatial frequency domain, known as K-space. Each line, after being scanned, is added to the K-space; this is known as K-space filling. From the K-space we can then easily convert the spatial spectrum to the final image using a Fourier transform [7] [10].

In MRI, the resolution is defined by the size of the imaging voxels. Since voxels are cubes, the resolution can vary in each dimension. The resolution depends on the K-space size, field-of-view (FOV) and slice thickness. K-space size is the number of frequency-encoding steps times phase-encoding steps, therefore, the more steps, the higher the resolution. Field-of-view is the size of the object we are sampling; the bigger it is, the smaller the resolution will the resulting image. Lastly, slice thickness depends greatly on the strength of the G_{sl} and on the frequency bandwidth of the RF pulse we apply.

Usually the slice thickness is the weakest factor, providing resolutions such as 1x1x3 mm. Since in fMRI imaging we want to detect time courses of brain activity, high temporal resolution is favorable. Given that high sampling rate, and therefore,

high resolution is time consuming, fMRI uses images of a smaller resolution, as opposed to anatomical MRI images [7] [10].

2.9 Echoplanar Imaging

Echoplanar imaging (EPI) is an upgrade of GRE imaging, making it the fastest acquisition method available. Essentially, the concept lies in the rapid changing of the phase-encoding and the frequency-encoding gradients, resulting with filled K-space within a few tens of milliseconds, as shown in figure 2.5 [7] [10].

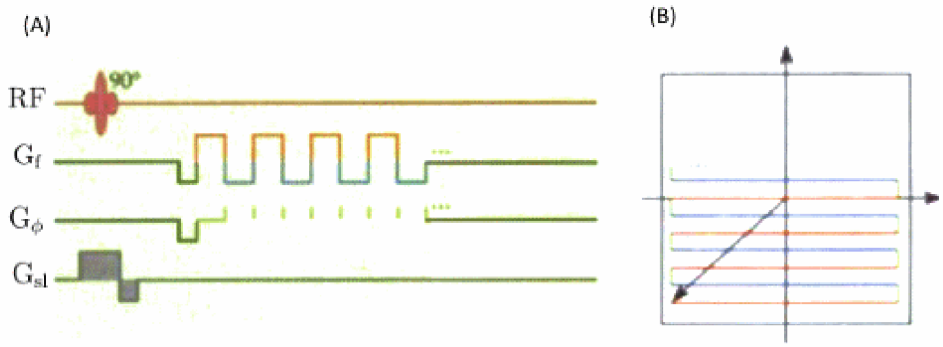

Fig. 2.5: Illustration of an EPI pulse sequence (A) and its zig-zag trajectory in the K-space (B) [7]

3 BOLD FMRI SIGNAL

Blood oxygenation level dependent (BOLD) fMRI is a method that indirectly, by the means of different magnetic properties and concentrations of oxyhemoglobin and deoxyhemoglobin, measures metabolic activity in the brain [7] [10].

3.1 Consequences of Neural Activity

The processing of information in a neuron or resending the information further along consumes a considerable amount of energy, which then needs to be returned. ATP (adenosintriphosphate) molecules, that serve as small sources of energy, can be formed after providing glucose and oxygen from the blood to the neuron. While glucose molecules are freely transported by blood, oxygen molecules are bound to hemoglobin. After the neuron is excited, it increases its incoming blood flow which carries these sources for creating ATPs. Glucose and the oxygenated hemoglobin (oxyhemoglobin) then enter the cell and the hemoglobin binds any waste carbon dioxide. This oxygen-free hemoglobin is referred to as deoxyhemoglobin [7] [10].

3.2 Magnetic Susceptibility and the Origin of the BOLD Signal

In our bodies there are a lot of molecules that have either diamagnetic or paramagnetic properties that can locally change the field strength. This can lead to geometric disturbances of the image and local signal losses. The extent to which either diamagnetism or paramagnetism of a molecule is disturbing the signal is known as magnetic susceptibility.

The detection of local changes in the concentration of oxyhemoglobin and deoxyhemoglobin in the BOLD fMRI is based on this phenomenon. While oxyhemoglobin is only sligthly diamagnetic, deoxyhemoglobin is strongly paramagnetic, causing dramatic perturbations in the local homogeneity of the magnetic field. As a result, this leads to dephasing of the spins (rapid T_2^* decay) and, therefore, loss of the signal [7] [10].

3.3 Hemodynamic Response Function

Contrary to what one might assume, the neuronal activity is not detected by the loss of the MR signal, but instead by the resultant increase in the signal. There are many theories accounting for this signal increase; the most widely accepted theory states

that the oxyhemoglobin displaces the deoxyhemoglobin that had been suppresing the signal intensity.

As we can see in figure 3.1A, the bloodflow changes very slowly, causing a delayed increase in the BOLD signal of about 2 - 3 seconds after onset of the neuronal activity. Furthermore, even after the activity of the neuron ceases, the oxygenated blood keeps flowing to the region with active neurons. This superfluous perfusion of the oxygenated blood accounts for a prolonged signal response of about 15 - 25 seconds. The resulting change in the signal strength between the active and nonactive voxels is very small, only a few percent, making the detection of the brain activity very difficult to distinguish (figure 3.1B) [7] [10].

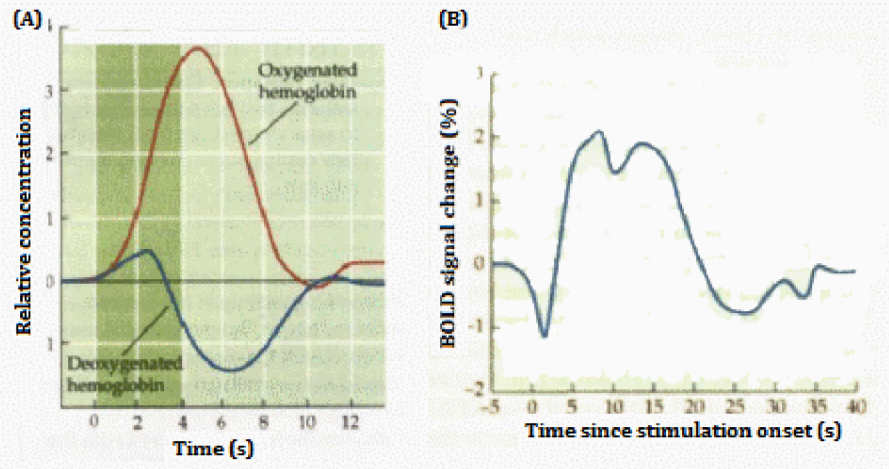

Fig. 3.1: (A) Changes in the concentrations of oxyhemoglobin and deoxyhemoglobin after neuronal activity and their impact on the BOLD signal (B) [7]

3.4 Experiment Setups

In BOLD fMRI experiments we measure either the resting state activity of the brain or the response of the brain to presented stimuli. However, as stated in the previous section, brain activity induces only very small changes of about a few percentage points in the recorded signal and detection is thus very difficult. To overcome this problem stimuli are presented repeatedly and their signal responses are aggregated to enhance the difference between the active and non-active regions of the brain [7].

For the stimuli-induced experiments there are 3 main types of design: block, event-related and mixed.

In the block design, the stimulus is presented in a block lasting about 20 seconds, during which the HRF (hemodynamic response function) reaches its peak in the signal, and is followed with a null-block that lasts approximately the same amount of time. Block designs offer good detection power, but poor estimation power (i.e. weak ability to describe the time course of the HRF response).

In the event-related design the two sets of stimuli are usually presented in a random fashion for a very short time. Contrary to the block design, the estimation power is very good. The detection power depends on the number of stimuli we present and aggregate [7].

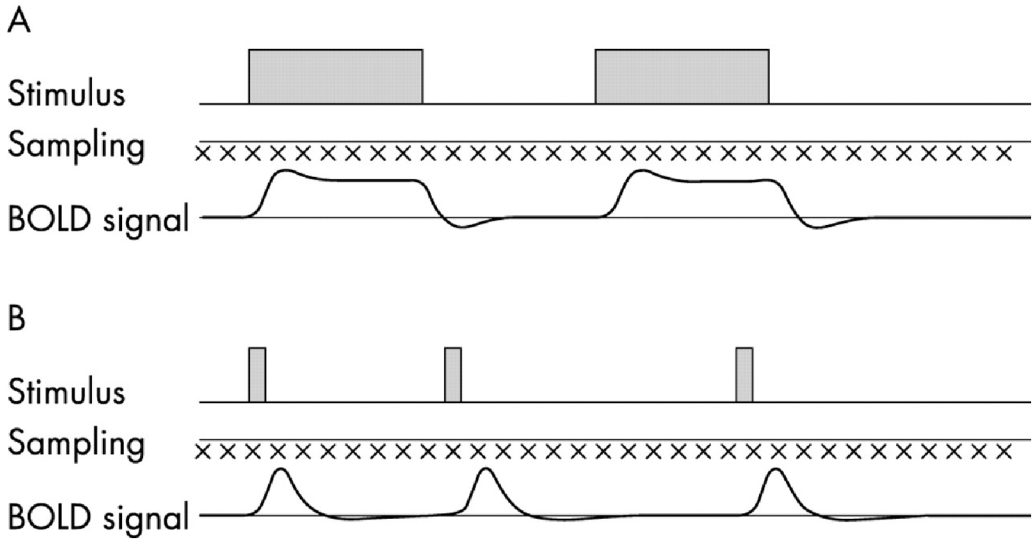

Fig. 3.2: Schemes of a block design (A) and an event-related (B) design.

4 NOISE AND ARTIFACTS

The signal we detect is comprised of not only the utilizable signal, but also of additional noise and artifacts that corrupt the quality of the signal and of the resulting image. In this chapter a few of the most abundant sources of such signal distortion are listed.

4.1 Chemical Shift Artifact

Chemical shift is caused by the different magnetic susceptibility of different tissues. Magnetic susceptibility changes the precessing frequency of nuclei and, therefore, they appear as if they were shifted in space (recall equation 2.2). In reality this means we see shadows and brightness around the edges of tissues having distinctly different magnetic susceptibility. In brain images the chemical shift is most significant at voxels near transitions between cerebrospinal fluid and white/gray matter [7] [10].

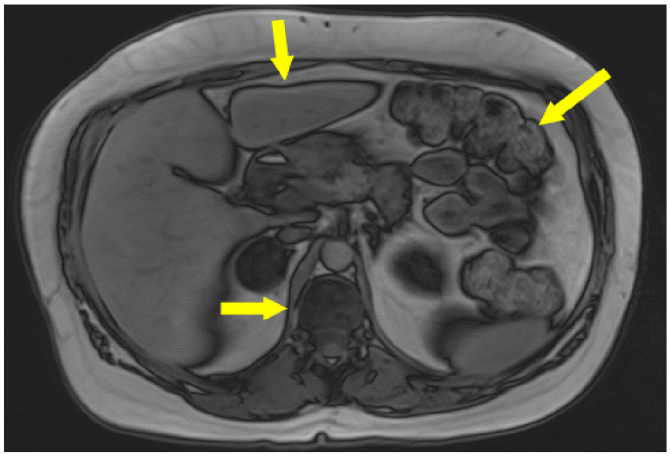

Fig. 4.1: Chemical shift artifact: note the dark edges marked by the yellow arrows.

4.2 Thermal Noise

All functional and anatomical MRI data are to some extend affected by thermal noise, which is caused by the heat-related motion of electrons. The acquired signal travels in the form of an electric current through a series of conductors, amplifiers, resistors and other components of the MRI scanner. In each of the components, free electrons collide with atoms, thus exchanging energy. This collision leads to the distortion of the electric current and the signal. The higher the temperature

of the system is, the more frequent the collisions are, resulting in higher noise and distortion of the data. For this reason, every MRI scanner is constantly cooled down by liquid nitrogen to minimize the motion of the electrons [7] [10].

4.3 System Noise

System noise in the MRI scanner represents discrepancies in the functioning of the hardware. Such discrepancies can be found in the inhomogeneity of the gradient magnetic fields and the static magnetic field; the latter having a particularly negative effect, known as scanner drift. Even though these discrepancies, or changes, in the static magnetic field might be very small (tenths of a part per million per day), the resulting impact on the resonant frequency is much greater, changing it on the scale of a few hertz. This can lead to changes in the signal intensity over time. Similarly, discrepancies in the gradient magnetic fields can lead to geometrical distortions in the image and changes in the slice selections over time [7] [10].

4.4 Physiological Noise

Periodical cardiac pulsation and breathing also produce changes in the signal and small motion artifacts. Respiration causes variability in the fMRI data: as the lungs expand and the oxygenated blood rushes into the brain it causes a wave of magnetic susceptibility and alternation in the homogeneity of the magnetic field. Furthermore, both cardiac pulsation and respiration induce small movements of the subject.

One might suppose that filtering out cardiac pulsation and breathing may be easy due to their periodicity. This might be true for the breathing effects, as the sampling rate of TRs is typically, with modern MR scanners, under 2500 ms. On the other hand, however, the subject might also breath very fast, which might result in an undersampling of the breathing effects. Moreover, for effective sampling of cardiac pulsation the TRs would have to be even faster, shorter than 500 ms. Since in practice such rapid sampling is not achieved, the data are corrupted by the aliasing of the cardiac pulsation and breathing [7].

4.5 Motion Artifacts

The motion of the subject represents the most frequent and drastic distortions of the data in two ways: it changes the locations of the voxels and alters the signal properties. In addition to wholebrain analysis, voxel-by-voxel statistical analysis

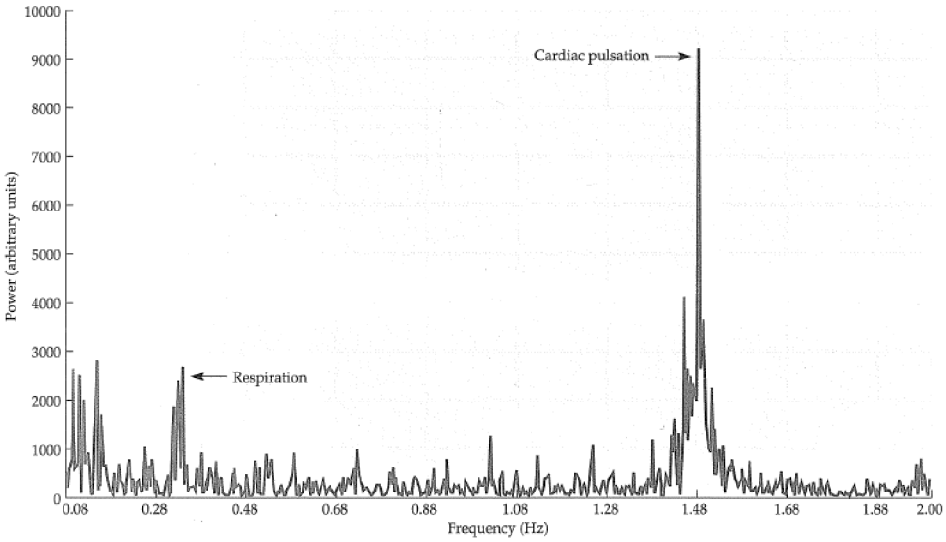

Fig. 4.2: Power spectrum of a voxel during an experiment. Cardiac pulsation and breathing were sampled effectively due to the fast TR of 250 ms [7]

is often employed. Therefore the voxels have to correspond to the same locations during the entire experiment. Only in this way can we analyze the time courses of certain sets of neurons within a region of the brain. If the voxels do not correspond to the same location over time, in an extreme case we might find ourselves running statistical tests on voxels that are, for instance, alternating their locations between white matter and cerebrospinal fluid. Such voxel shifts can as a consequence, lead to false-positive and false-negative errors in statistical tests - voxels suddenly change their intensity as if they were in the brain's active region.

The higher the resolution is, the smaller the voxels are and, hence, the more motion-susceptible the image is. In the best cases, small head motions can be corrected during preprocessing. However, larger movements can make the correction impossible, leading to the removal of a whole series of scans from the dataset.

As the subject moves, it not only changes the locations of the voxels in respect to the brain region, but it also interferes with the magnetic gradients and slice selection process. When a certain slice is excited and the subject moves his head, it might happen that the next slice to be selected will include a section of the previous slice and excite it again. However, since this section did not reach full T_1 relaxation, the signal from this section will be smaller and T_1 weighted, accentuating contrast for different tissues. This effect is referred to as spin-history artifact [7] [10] [15].

The next important implication of motion artifact is the rise of spurious variance that tends to be more similar in nearby voxels. This would not be a problem

in task-evoked experiments, however, a considerable amount of fMRI experiments focus on resting state fMRI, which uses corelation analyzes for the functional connectivity mapping of the brain. In the past few years many research groups have found out that the young and the elderly exhibit underconnectivity as opposed to young adults. For instance, children and the elderly showed weak signal correlations between distant regions of the brain and stronger ones between the nearby regions. However, retrospectively, a lot of such observations were found to be invalid due to motion artifact, which increases local correlations, and the fact that children and the elderly are usually more susceptible to motion [17] [20].

5 FMRI DATA PREPROCESSING

Before any statistical tests are performed, the raw data first has to be preprocessed. Preprocessing ameliorates the data quality by diminishing artificial signal variability and correcting it for motion.

Since preventing motion from occurring is much easier than subsequent analytical corrections, the subject is instructed to stay still before the experiment begins. However, this might be very difficult due to the length of the experiment, which can stretch up to 20 minutes or longer. For this reason, the researches provide the subjects with head restraints, such as masks, vacuum packs or bite bars, which are the most effective, but least favorite and bearable. However, even when using such restraints some motion is still present.

Usually the first preprocessing step represents realignment of the scans affected by motion. Next is the coregistration of the anatomical and functional images to obtain images which can better trace the anatomical sources of the brain activity. The another step that usually follows is time correction, which tries to interpolate the time courses of the BOLD responses within each of the slices, which were acquired with certain time lags, and adjust them as if they were acquired at the exact same moment. In case there is a desire to make comparisons between subjects, it is necessary to first transform the images of each subject to the same template, so that each brain more or less has the same anatomy. Spatial filtering and intensity normalization are other steps that are almost always performed. Lastly, if the sampling frequency is high enough, respiratory and cardiac pulsation artifacts can be removed by temporal filtering the time courses of the BOLD signal [7] [12].

5.1 Head Motion Correction

To align (or coregister) the scans in a way that each voxel corresponds to the same brain region over time, rigid body transformation is used. Rigid body transformation is a spatial transformation, which supposes that the object (e.g. scans of the brain) to be oriented does not change its shape over time. This condition is attained by correcting the motion for one subject. The transformation then reorients the object in three translations (i.e. moving the scan in x-,y-, and z-axes) and three rotations (i.e. rotating the scan around x, y, and z axes; also known as pitch, roll and yaw). The scans are coregistered with a reference image, which is usually the mean image of the scans [7] [12].

The computer first calculates many sets of possible coregistrations, from which only the right one has to be chosen. To do this the computer calculates a mathematical measure known as cost function for each coregistration. Ideally, the cost

function would be zero if the image had the same voxel intensity and was aligned perfectly. Therefore the right scan has the minimum cost function value [7].

At the end of the coregistration process a matrix with 3+3 columns of translational and rotational parameters by N rows, where N is the number of scans, is obtained. The time courses of the translational and rotational parameters are known as motion regressors [7] [12].

To describe coregistration mathematically the above-mentioned process can be rephrased as following: assuming the image to be oriented $\Omega(x)$ and the reference image $\tau(x)$ do not change their shape over time, rigid body, six-parameter affine spatial transformation $q(x,\gamma)$ can be used. This transformation is a vector function of position in space x, defined by the six parameters of a rigid body transformation $\tau = [\tau_1....\tau_6]$, where [5] [14]

$$\beta \cdot \tau(x) \approx \Omega(q(x,\gamma)) \tag{5.1}$$

and β is a scaling constant. Assuming the images are smooth (or they can be filtered with a lowpass filter), function $q(x,\gamma)$ can be further expanded in terms of six vector functions $\gamma_k \partial q(x,\gamma)/\partial\gamma_k$ of x, approximating the six parameters of a rigid body transformation [5]

$$q(x,\gamma) \approx x + \sum_k \frac{\gamma_k \partial q(x,\gamma)}{\partial \gamma_k} \tag{5.2}$$

After substituting this derivation to equation 5.1 [5]

$$\beta \cdot \tau(x) \approx \Omega\Big(x + \sum_k \frac{\gamma_k \partial q(x,\gamma)}{\partial \gamma_k}\Big) \tag{5.3}$$

If $\Omega(x)$ is smooth the effects of the transformations $\gamma_k \partial q(x,\gamma)/\partial\gamma_k$ will not interact significantly. Therefore, the right side of equation 5.3 can be expanded using Taylor's theorem, neglecting high order terms as [5]

$$\beta \cdot \tau(x) \approx \Omega(x) + \sum_k \frac{\gamma_k \nabla_x \Omega(x) \cdot \partial q(x,\gamma)}{\partial \gamma_k} \approx \Omega(x) + \sum_k \frac{\gamma_k \partial \Omega(q(x,\gamma))}{\partial \gamma_k} \tag{5.4}$$

This equation states that the difference between a reference and an object image can be expressed as the sum of the changes in the object image for each parameter times the amount of that parameter. The equation can be further expressed in matrix notation as [15]

$$\Omega \approx G \cdot [b\gamma]^T, \quad \text{where} \quad G \approx [\tau - \partial\gamma/\partial\gamma] \tag{5.5}$$

γ and Ω are column vectors with one element per voxel and b is an estimate of β. In practice it is easy to calculate the six columns of $\tau - \partial\gamma/\partial\gamma$ by applying small translations and rotations to the object image Ω and measuring the changes in voxel values. The vector γ of the six parameters corresponds to the estimated translations and rotations; it is estimated in a least square sense by [15]

$$[b\gamma]^T = G \cdot (G^T \cdot G)^{-1} \cdot G^T \cdot \Omega \tag{5.6}$$

After these six transformation parameters are obtained, the image is re-sampled (spatially interpolated) onto the same grid of voxels as the reference image Ω.

The tranformation T_i is an iterative process of a series of scans, where i denotes one individual volume $\Omega(x)$ and T_i coregisters this volume to the reference frame $\tau(x)$. Each transform can then be expressed as a combination of rotation and translation parameters as following [15]

$$T_i = \begin{bmatrix} R_i & t_i \\ 0 & 1 \end{bmatrix} \tag{5.7}$$

Here R_i is a 3×3 rotation matrix and t_i is a 3×1 column vector of displacements. R_i is divided into three elementary rotations: pitch, yawn and roll. Therefore, $R_i = R_{i\alpha} \cdot R_{i\beta} \cdot R_{i\gamma}$, where [15]

$$\begin{aligned} R_{i\alpha} &= \begin{bmatrix} 1 & 1 & 0 \\ 0 & \cos(\alpha_i) & -\sin(\alpha_i) \\ 0 & \sin(\alpha_i) & \cos(\alpha_i) \end{bmatrix} \qquad R_{i\beta} = \begin{bmatrix} \cos(\beta_i) & 0 & \sin(\beta_i) \\ 0 & 1 & 0 \\ -\sin(\beta_i) & 0 & \cos(\beta_i) \end{bmatrix} \\ R_{i\gamma} &= \begin{bmatrix} \cos(\gamma_i) & -\sin(\gamma_i) & 0 \\ \sin(\gamma_i) & \cos(\gamma_i) & 0 \\ 0 & 0 & 1 \end{bmatrix} \end{aligned} \tag{5.8}$$

Note that there are more types of interpolation varying in the computational complexity and the quality of interpolating. The least computationally complex interpolation is linear interpolation, which uses information of voxel values for only the 4 immediate neighbours. However, this method is also relatively inaccurate and achieves poor results. In contrast, other methods such as sinc interpolation achieve superb results, however, they are ruled out (in our case) because of their high computational complexity. The most frequently used method for re-sampling the image is B-spline interpolation, which represents a compromise between the quality of interpolation and computational complexity [7].

5.2 Slice Acquisition Time Correction

FMRI analysis assumes that the scans were obtained at one exact moment. However, in reality the scanning process begins, for instance, at the top slice of the brain and iteratively descends to the bottom part of the brain. This causes time lags between the slices, the most profound being between the first and the last slices. The delay depends on the speed of the image acquisition, with EPI TR being about 2 seconds long. As a result, reflecting the HRF, this delay may cause dramatic differences between recorded signals of the individual scans [7] [12].

To correct these time discrepancies, the time courses of the HRFs are interpolated and adjusted to have the same time offsets. Though this might seem like a perfect solution, the longer the TRs are, the greater the interpolations are and, hence, the greater the chance of errors in the interpolations [7] [12].

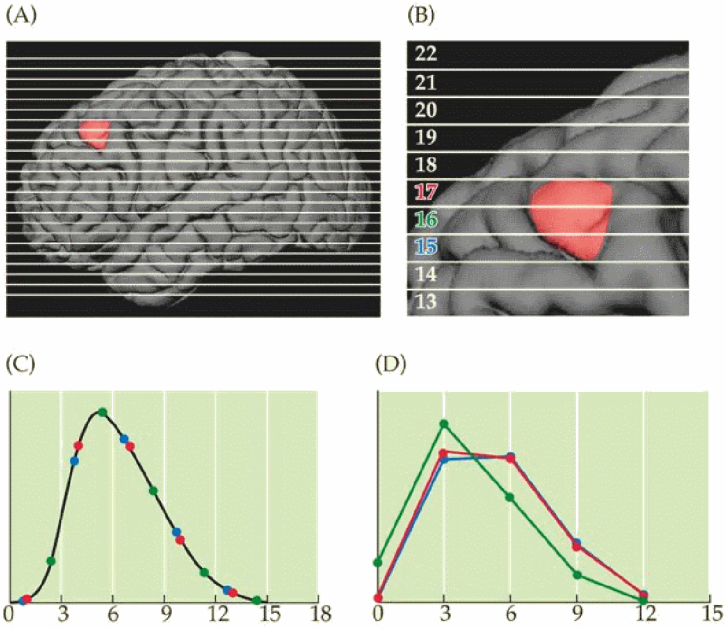

Fig. 5.1: The scans of the active region in the brain (A) are acquired with a standard interleaved sequence (B). Because these slices are acquired at different times, the hemodynamic response within the slices will have very different time courses. The actual recorded signal from the different slices is shown in (C). When plotted for each TR, there are different time courses for the slices acquired early in the TR and the slices acquired later (D). [7]

5.3 Spatial Normalization

Since human brains vary remarkably in their anatomy, they have to first be transformed into a uniform template (or space) before any statistical tests are executed. This process is known as spatial normalization. In addition to rigid-body transformation, normalization also allows for possible stretching, squeezing and warping of the images of each brain, transforming them into approximately the same anatomical structure. Nowadays, the most frequently used reference template is Montreal Neurological Institute (MNI) space, which was derived from an average of MRI anatomical images from hundreds of individuals [7] [12].

5.4 Spatial Smoothing

Spatial Filtering is used to improve the signal to noise ratio. In addition, it also attenuates the interindividual variability in the brain anatomy and eliminates interpolation errors from the acquisition time correction process and small motion artifacts. On the other hand, it lowers the effective spatial resolution and, in the worst case, it can cause false negative errors in the ensuing statistical analyzes.

The smoothing is usually done with a Gaussian filter, whose value of full width at half maximum (FWHM) can be from 6 to 10 mm [7] [12].

5.5 Temporal Filtering

Filtering the time courses of the BOLD signals for each individual voxel can substantially improve the SNR. A highpass filter is usually used to remove drifting of the signal. Combining it with a lowpass filter, a respiration artifact (12 breaths per minute $\Rightarrow$ f = 0.2 Hz) can be removed: TR of EPI is about 2 seconds $\Rightarrow$ $F_{sampling}$ = 0.5 Hz. Therefore the Nyquist–Shannon sampling criterion is met. However, it is not possible to eliminate the cardiac pulsation artifact (60 beats per minute $\Rightarrow$ f = 1 Hz) [7] [12].

6 REGRESSION ANALYSIS OF BOLD FMRI DATA

After the BOLD fMRI data are preprocessed, they are statistically tested to provide the answer as to whether our tested hypothesis is valid or not. One of the most frequently used statistical methods for such tests is multiple regression analysis. The core idea of multiple regression analysis is that the response of the brain activity to presented stimuli during an experiment is predictable. The predicted model is then composed of several regressors, which are essentially the predictions (i.e. independent variables) we made about the time courses of the brain activation. Ideally, the sum of all the regressors should fully explain the real brain activity we measured in the experiment [7].

$$y = \beta_0 + \beta_1 * x_1 + \beta_2 * x_2 + ... + \beta_n * x_n + \varepsilon \tag{6.1}$$

The regression models as shown in equation 6.1 have only one known quantity: the experimental data (y). The regressors (x_i) might or might not contribute to the data, depending on the parameter weights (β_i), which reflect the scale of contributions of individual regressors. β_0 is a constant, which corresponds to the baseline signal intensity. The last parameter, (ε) is residual error; a part of data that could not be explained by any regressor. An example of the matrix of regressors, known as design matrix, is shown below in figure 6.1 [7].

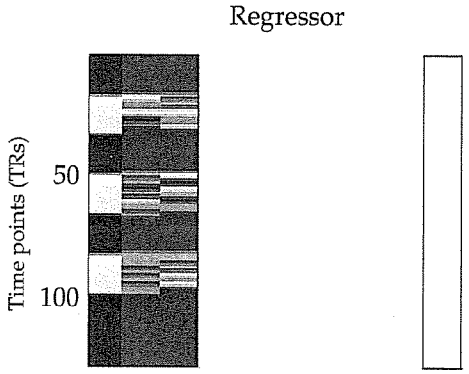

Fig. 6.1: A design matrix for General Linear Model (see below). Three regressors are constructed for mixed block/event-related design. The first column represents a blocked effect, while the other two represents the event-related effects to two different presented stimuli. Note that the white bar on the right represents the constant value in the data, removing the mean signal intensity. [7]

6.1 General Linear Model

The most frequently used class of statistical tests of the multiple regression analysis is the general linear model (GLM). This method is employed either in 1st level analysis, which evaluates the data of a single subject, or in 2nd level analysis, which evaluates the data across a tested group of subjects. In order to perform the 2nd level analysis images need to be, in addition to preprocessing, also spatially normalized to a common space, such as MNI.

In practice, the equation 6.1 above is replaced with a set of matrices as shown in figure 6.2. The fMRI data are represented as a matrix consisting of n time points (rows) by V voxels (columns). Note that the spatial structure of the fMRI data is not considered, the statistics focus only on the time courses of voxels. The design matrix is comprised of M regressors (columns) by n time points (rows). This design matrix is multiplied by a parameter matrix, which contains M parameter weights (columns) by V voxels (rows). Finally, the error matrix, which contains V voxels (columns) by n time points (rows), accounts for the unexplained error of each voxel [7].

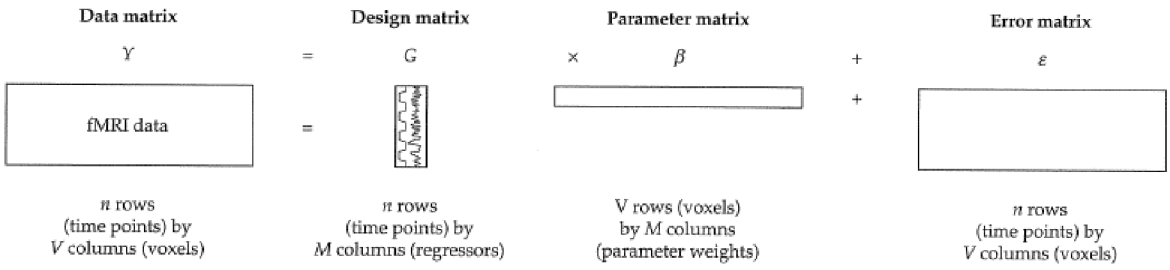

Fig. 6.2: General linear model tries to explain the original data (Y) by calculating parameter matrix β, which would provide the best fit for the design matrix (G) by minimizing the unexplained error ε [7]

From a statistical point of view all the efforts of sustaining the homogeneity of the magnetic field, avoiding all sorts of artifacts and preprocessing the data are ways of how to minimize the residual errors ε in the error matrix. In addition, the design of the experiment plays an equally important role as to a simplification the construction of regressors .

As mentioned earlier, each voxel value can be represented as

$$y = \sum_{i=1}^{k} x_i + \beta_i + \varepsilon_i \tag{6.2}$$

where y is the signal intensity and k is the number of regressors in the design matrix. Subsequently, based on the time courses of the signal intensity y and correlated regressors, β values of the parameter matrix can be calculated in a least square sense by [14]

$$\beta = (x^T x)^{-1} x^T y \tag{6.3}$$

A t-statistic, from which statistical parametric maps of brain activity are constructed, can then be performed by dividing the contrast of the estimated parameters $c^T\beta$ by the standard error of this estimate. The standard error is based on the variance of residuals (variance unexplained by the model) and the specific portion of the covarinace matrix. [14]

$$T = \frac{c^T\beta}{\sqrt{\delta^2 c^T x^{-1} v x^{-T} c}} \tag{6.4}$$

6.2 Regressors

Regressors can be divided into regressors of interest (see 6.1), which predict the researcher's expectations about the brain activity, and nuissance regressors, which, on the other hand, account for certain errors in the data. Nuissance regressors are mostly used for motion correction, explaining data distortions for translation and rotation motions. Moreover, if the motion is extreme and drastically corrupts the data of certain scans, the scans are to be excluded from the statistics by constructing single timepoint nuisance regressors (also known as scan nulling or spike regressors). These regressors omit such motion-affected scans from analyzes by assigning them non-zero values, which accounts for all the variability of that volume. The downside of constructing a wide range of regressors, and thus modeling a great portion of the signal, is the reduction of the degrees of freedom. As a result, the statistical reliability of the tested hypotheses is reduced. Therefore, the number of nuissance regressors used is limited [7] [9] [18] .

Assuming the HRF is treated as a filter, task regressors can be constructed as a convolution of Delta functions with the HRF. This approach is identical to the Finite Impulse Response (FIR) model used in signal processing. An example of such a model is shown in figure 6.3 [19].

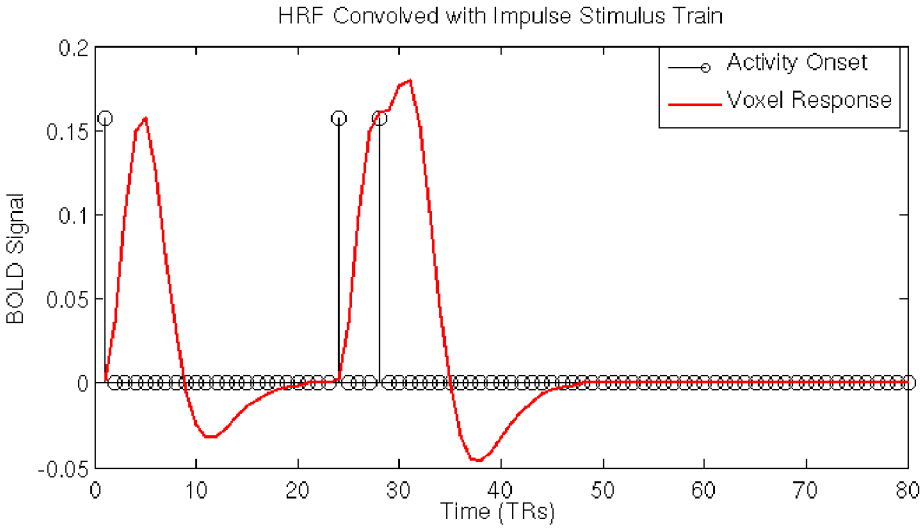

Fig. 6.3: Modeling a task regressor using an approach identical to modeling a FIR filter: convoluting HRF with Impulse Stimulus Train [19]

7 DETECTION OF MOTION-DISTURBED DATA

Subject movement is often measured with summary statistics, yielding data quality indices. Such statistics can be based on the motion parameters described above or on the change of intensity between the time courses across voxels (DVARS). Another possibility is tracking the movement of a subject with a camera. However, the equipment has to be MR-compatible, and, therefore, this method is very expensive and rarely employed. In practice, the most frequently used method is the combination of two indices, FD and DVARS. These can be used to flag scans of suspect quality to be ignored when performing calculations upon the data and thus creating temporal masks of the data. An important point to consider is the detection limits of these indices, as different datasets can be best fitted using different thresholds. This results in the disunity in the quantification of such thresholds across studies.

As the motion artifacts cannot be fully regressed out in GLM due to the spin-history artifact, summary statistics is often used to describe the extent of subject motion and to decide whether to discard a scan showing excessive motion or not. Furthermore, if a subject exhibits constant movement throughout scanning, it is worth considering whether it would not be better to discard the entire data of that subject [15] [16] [7] [9].

7.1 Motion Regressors

The six motion parameters obtained from rigid body transformation can be used for evaluating the extent of subject motion. In addition to those six parameters, other derivative parameters can be calculated. For instance, the difference between values of translational (d_{xi}) and rotational (Θ_{ri}) parameters of successive voxels is calculated as [15]

$$\Delta d_{xi} = d_{x(i-1)} - d_{x(i)}, \quad \Delta\Theta_{ri} = \Theta_{r(i-1)} - \Theta_{r(i)} \tag{7.1}$$

or sometimes this contrast of motion parameters is further enhanced by calculating the square of the difference [2]

$$\Delta d_{xi}^2 = (d_{x(i-1)} - d_{x(i)})^2, \quad \Delta\Theta_{ri}^2 = (\Theta_{r(i-1)} - \Theta_{r(i)})^2 \tag{7.2}$$

Those motion regressors, 36 in total, can be included into the GLM as nuissance regressors. However, as mentioned in the previous chapter, this can lead to the decrease of the statistical reliability.

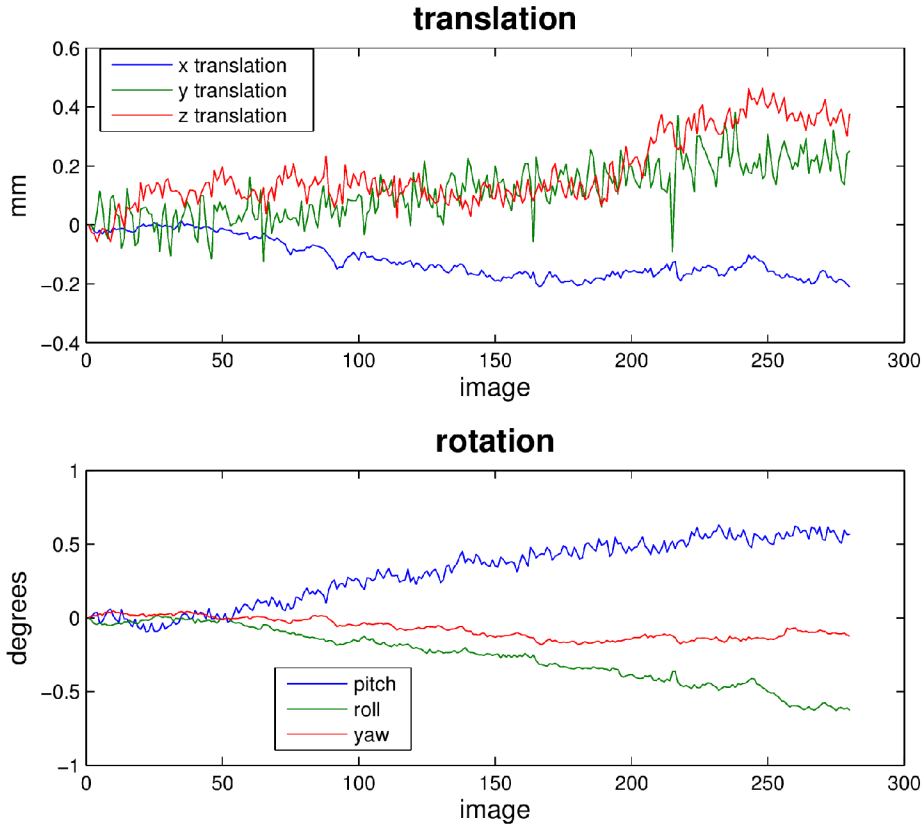

Fig. 7.1: Motion parameters obtained from rigid body transformation

7.2 FD

For summarizing the extent of a movement, the motion regressors per se are a bit of an awkward measure. Instead, instantaneous head motion is expressed by a single scalar quantity, known as framewise displacement (FD). Although there are more approaches as to calculate FD, the most frequently used formula, derived by PhD. J. D. Power, is as follows [15]:

$$FD_i = |\Delta d_{ix}| + |\Delta d_{iy}| + |\Delta d_{iz}| + |\Delta d\alpha_i| + |\Delta d\beta_{iz}| + |\Delta d\gamma_i| \tag{7.3}$$

where $\Delta d_{ix} = d_{(i-1)x} - d_{ix}$ and similarly for the rest of rigid body parameters $[d_{ix} \quad d_{iy} \quad d_{iz} \quad d\alpha_i \quad d\beta_{iz} \quad d\gamma_i]$. The rotational parameters were converted from degrees to millimeters by calculating displacement on the surface of a sphere with a radius of 50 mm, which is approximately the mean distance from the cerebral cortex (where the activity is measured) to the center of the head (i.e. the axis of rotation). The formula for this conversion is [15]

$$d\alpha_i = (50 * \frac{\pi}{180})\alpha_i \tag{7.4}$$

7.3 DVARS

DVARS stands for derivative (D) of timecourses, root mean squared variance over voxels (VARS). In other words, DVARS measures the change of a BOLD signal intensity from one volume to the next by calculating backward differences within a spatial mask at every timepoint. Although this change of intensity between two timepoints of a voxel is not a direct measure of motion, DVARS is a very accurate motion indicator; the formula for DVARS whole-brain mask is [15]:

$$DVARS(\Delta I)_i = \sqrt{\langle [\Delta I_i(\overrightarrow{x})]^2 \rangle} = \sqrt{\langle [I_i(\overrightarrow{x}) - I_{i-1}(\overrightarrow{x})]^2 \rangle}, \tag{7.5}$$

where I is the intensity between two timepoints (or scans) i.

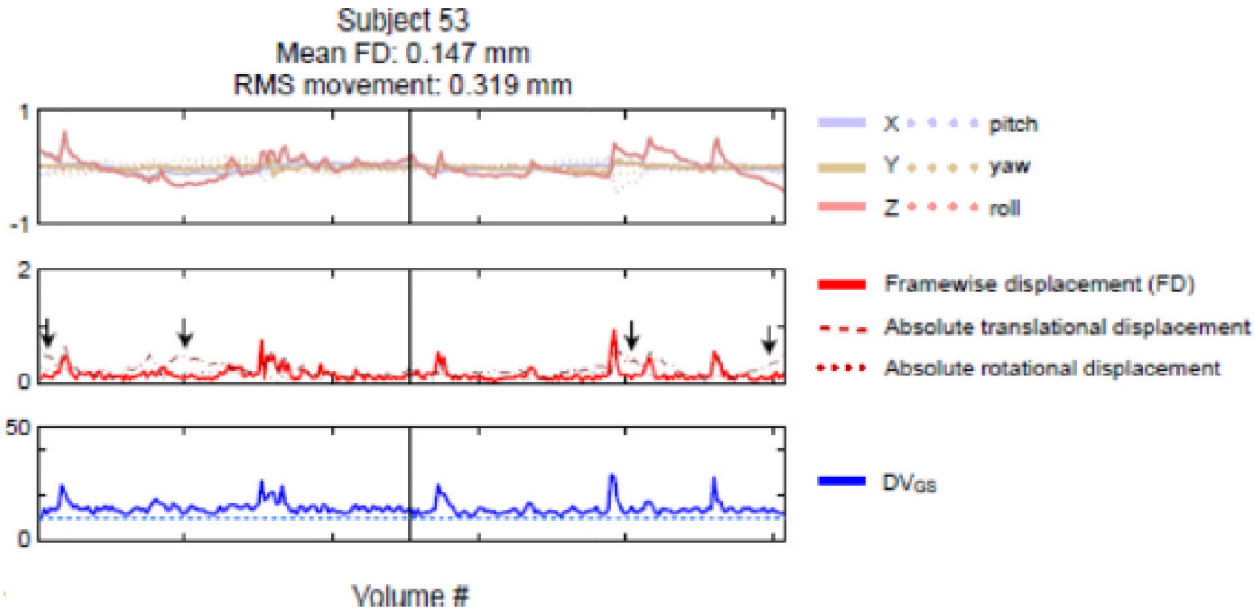

Fig. 7.2: Comparison of motion parameters, FD and DVARS

8 REMOVAL AND SUBSTITUTION OF MOTION-DISTURBED DATA

As previous studies have shown, motion artifact is not easily removable due to its nonspecific spectrum, affecting the signal on every frequency component (see figure 8.1). On the other hand, the effect can be attenuated by applying a narrow band pass filter (0.01 – 0.1 Hz instead of 0.008 – 0.1 Hz) and by including a high number of nuisance regressors; the greatest variance of the data was shown to be explained by the 36-parameter confound regression. Further analyses also showed that the parameters accounted only for the artifact, not for the actual HRF signals [18].

However, such prepocessing improvements only attenuates the motion artifact and does not remove it completely. To do so, the affected scans have to be omitted from further statistical analysis. In this thesis I will focus on the motion scrubbing method, introduced by Power et al. (2012), and spike regression [15] [18].

Note that there are several important approaches for motion artifact removal that I will not cover in this thesis, namely Independent Components Analysis (ICA) and Component Based Noise Correction Method (CompCor) [18].

8.1 Motion Scrubbing

As mentioned above, this method was introduced by Power et al. in 2012. The core idea of motion scrubbing lies in deleting scans displaying excessive motion by data quality indices (FD, DVARS). It is also advisable to remove one prior and two past scans, since the motion artifact is associated with a variety of transient signal changes. In his study, Power further argues that such removal has not been found to have any deleterious effects upon functional connectivity and on task fMRI. However, an alternative way that his team later adopted was to replace the affected scans with interpolations based on adjacent 'good' timepoints. As a previous study had argued (Carp, 2013), frequency filtering (basic preprocessing step) might spread the artifact into such adjacent 'good' timepoints and as a consequence motion scrubbing is done prior to the frequency filtering. Note that the motion scrubbing process can be done, along with re-calculating data quality checks, iteratively, possibly removing even more scans [16] [15] [3].

An especially intriguing question for which there is no resolute answer is the extent of data removal that is still acceptable for further analysis. The threshold adopted by most studies is 5 minutes of a 'good', uncensored signal. If a subject exhibits movements throughout scanning, his or her data are usually completely discarded [16] [15].

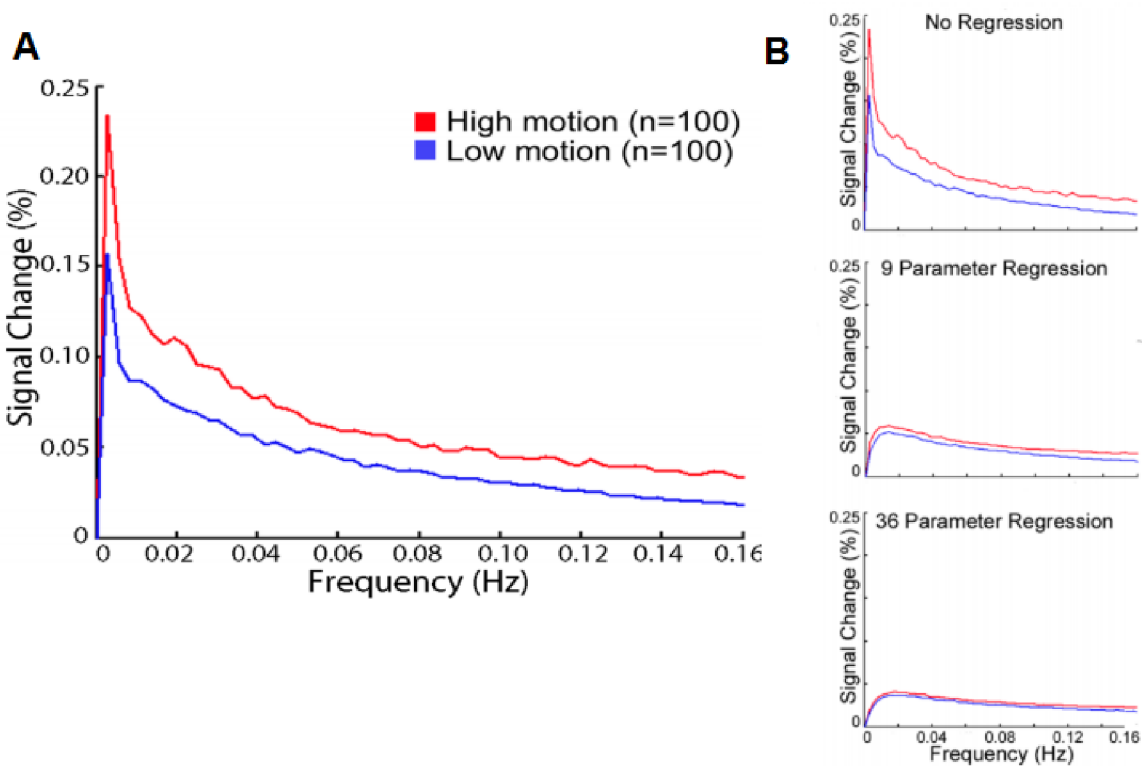

Fig. 8.1: A: analysis of the magnitude spectra of the matched low and high motion groups indicate that signal change introduced by in-scanner motion is relatively nonspecific in terms of its spectral characteristics. B: improved outcomes of signal preprocessing when applying a high number of regressors [18]

8.2 Spike Regression

Another way to remove (or neglect) motion-affected volumes is to construct so called spike regressors. These regressors, also known as nulling regressors, have null values throughout the time series except to the timepoints that are motion-affected; there the regressors have a value of one. As a result, they account for the variability of that motion-affected scan and thus discard it from further analysis. There is divided opinion among scholars as to the number of spike regressors that should be used; some studies claim that only one spike regressor should be used to discard the motion-affected volume; others argue that one should discard also one preceeding and the two following scans, as is done in the motion scrubbing method. However, overusing spike regressors could inevitably lead to reducing degrees of freedom and as a result reduce the reliability of that analysis. On the other hand, the advantage of spike regression to the motion scrubbing method lies in preserving temporal continuity and avoiding potential errors introduced by scan removal followed by temporal interpolation [9].

9 IMPLEMENTATION OF THE DETECTION AND MOTION-REMOVAL METHODS

The script is programmed in the MATLAB R2016a environment and uses SPM12 toolbox, version 6906. It works with 4D data in NIfTI format. The frame of the algorithm was was previously developed by my supervisor, Ing. Michal Mikl, Ph.D. He was kind enough to provide it to me. The frame consists of several blocks that preprocess given data. I implemented my extensions comprised of new lines and functions.

9.1 Chosen Indicators of Movement

For the actual script we chose FD and DVARS as metrics of movement; FD for its wide use in studies and DVARS as a complement that is also used very often. A comparison of FD and DVARS motion indicators is shown in the figure 9.1.

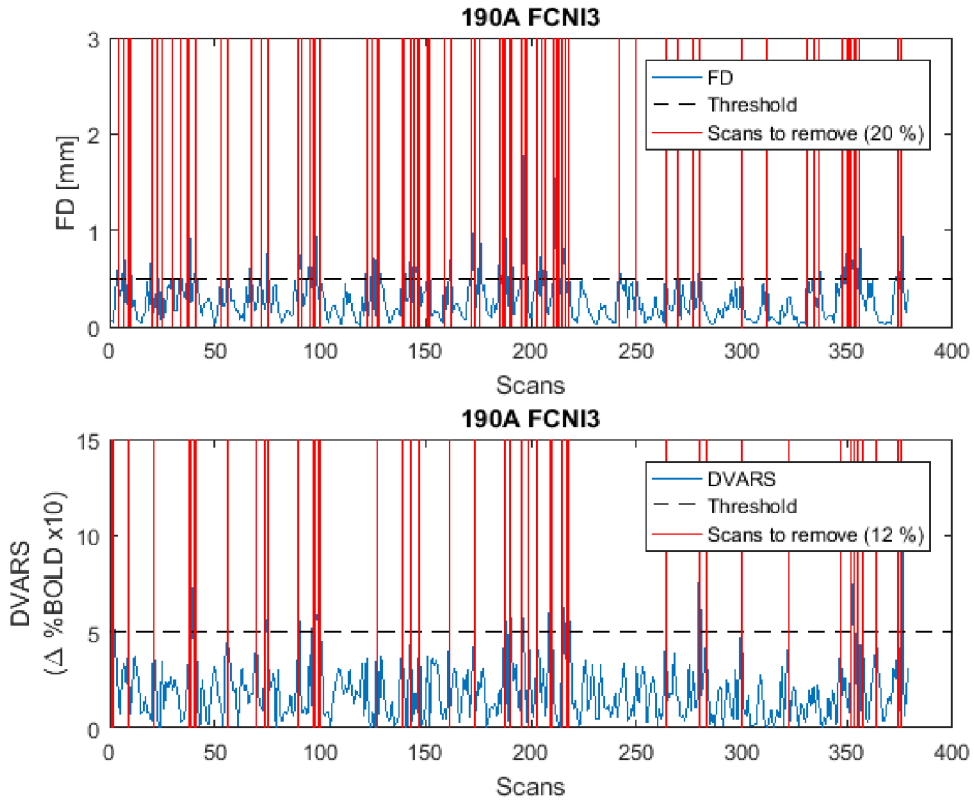

Fig. 9.1: Each metric yields a bit different output. Although in this particular case FD flagged more scans than DVARS, the distribution was random across the sessions (see supplementary materials chapter B).

As one can see, there is some overlap between the scans flagged by FD and DVARS. However, mostly there is a mismatch in both the positions of the flagged scans and their total number. Therefore, we decided to also use a fused combination of FD with DVARS.

9.2 Motion Regressor Matrices

For Spike regression, we came up with two designs of regressor matrices. With the first design regressing only the affected scan (0S-1S-0S), and with the second adding one preceding with and following scans to the affected scan (1S-1S-2S). The second design follows a study by Carp, 2013 [3].

DVARS_reg.value

	1	2	3	4	5
1	0	0	0	0	0
2	1	0	0	0	0
3	0	0	0	0	0
4	0	0	0	0	0
5	0	0	0	0	0
6	0	0	0	0	0
7	0	0	0	0	0

DVARS_reg3.value

	1	2	3	4	5
1	1	0	0	0	0
2	0	1	0	0	0
3	0	0	1	0	0
4	0	0	0	1	0
5	0	0	0	0	0
6	0	0	0	0	0
7	0	0	0	0	0

Fig. 9.2: At the top you can see the 0S-1S-0S design and at the bottom the 1S-1S-2S design. The affected scan here is scan number 2 (yellow). The 1S-1S-2S design also includes one previous and two following adjacent scans (marked in gray).

9.3 Motion Scrubbing

Unlike Spike regression, Motion scrubbing physically deletes the affected scans and replaces them with interpolation estimates. We decided to implement both linear and B-spline interpolations. This process takes quite a lot of computation time as

is shown in C.1.
Linear interpolation requires at least two good timepoints. The most difficult part of the implementation is to cover all possible cases: from extrapolating affected scans that are either right at the beginning or right at the end of the session to interpolating separately affected scans and scans whose adjacent scans are also affected.

As to the implementation, B-spline interpolation is similar to linear interpolation. It differs only in that it requires a minimum of four good timepoints.

10 DATA ANALYSIS

Both structural and functional data were acquired with the 3T Siemens Prisma MR scanner. The acquisition parameters of the functional data are shown in table 10.1. Anatomical T1-weighted images were acquired using a 3D sequence (240 sagittal slices, resolution 224 × 224, slice thickness = 1.0 mm, TR = 2300 ms, TE = 2.34 ms, FOV = 224 mm, flip angle = 8°).

In this work we used datasets FCNI1, FCNI3 and FCNI5; each accquired with different multi-band (MB) factors: MB factor = 1 (without MB acceleration), 4 and 8, respectively. All datasets comes from a block desing (recall 3.2) experiment with visual checkerboard stimulation during active period (A) and black screen during passive period (P) was used in all three runs. Each period lasted for 24 seconds and the periods were alternating as follows: PAPAPAPAPAPAP.

Tab. 10.1: Acquisition Parameteres of BOLD Data

	FCNI1	FCNI3	FCNI5
TR [s]	2.720	0.814	0.417
TE [s]	0.0300	0.0356	0.0356
Flip angle [°]	81	55	41
In-plane resolution	64x64	64x64	64x64
FOV [mm]	194x194	194x194	194x194
Number of axial slices	40	40	40
Thickness of axial slices [mm]	3	3	3
Number of scans	110	380	720
Multiband factor	1	4	8

10.1 Preprocessing of the Data

The following preprocessing was applied to each subject's time series of fMRI scans: a 6 parameter rigid-body realignment and unwarp of functional scans in order to correct for head movement; normalization to fit into a standard anatomical space (MNI), according to the anatomical image; and spatial smoothing using a Gaussian filter with a FWHM of 6 mm. The voxel size generated from these acquisition parameters was oversampled to 3 × 3 × 3 mm.

The overall design of the script is illustrated in a flowchart in figure 10.1.

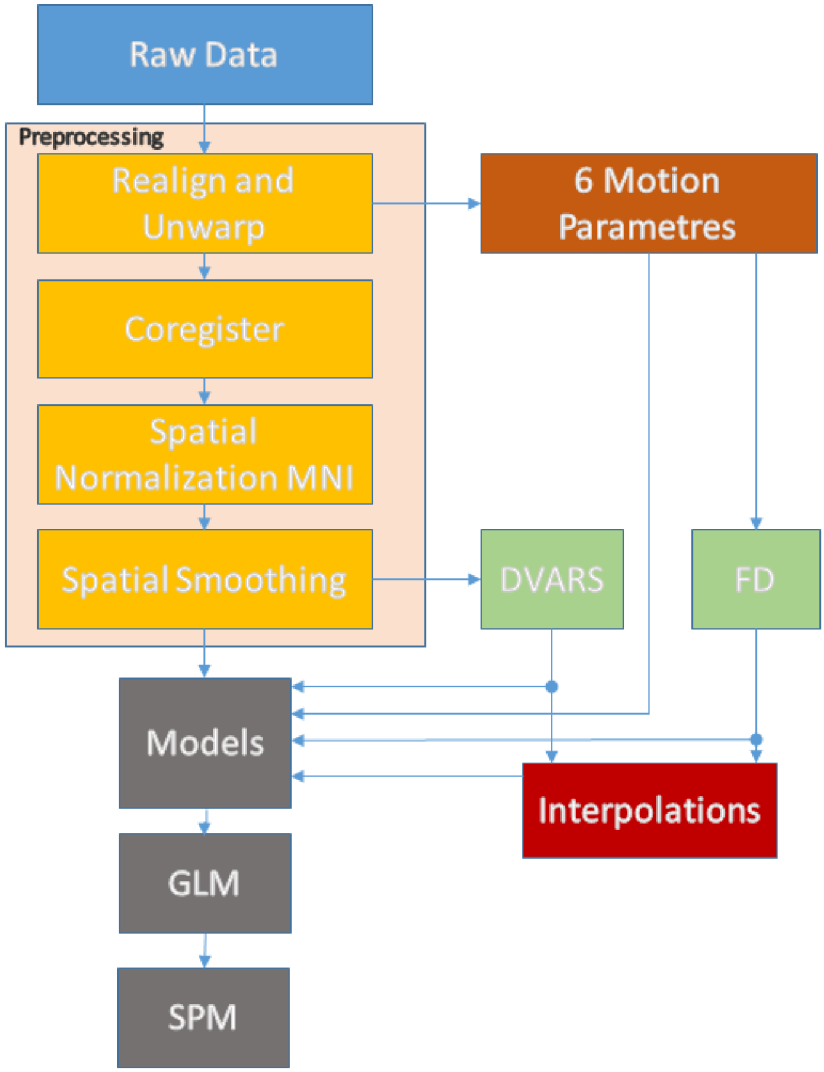

Fig. 10.1: First the raw data enters the preprocessing block from there the 6 motion parameters are obtained that are the basis for the upcoming FD computation. After the data finishes preprocessing, the DVARS indicator is computed, and the data enters interpolation computations, which follows FD, or a combination of FD with DVARS. The desired statistical models are then created and enter analysis.

10.2 Overview of Motion Prevalence in the Data

Motion prevalence in the data is summarized in table 10.2, along with an example of translational and rotational motion characteristics and derived FD and DVARS timecourses for subject 186A, session FCNI3, in figure 10.2.

Tab. 10.2: Overview of Motion Prevalence in The Data

Subject	Session	FD [%]	DVARS [%]
186A	FCNI1	-	-
	FCNI3	-	∼0
	FCNI5	-	-
190A	FCNI1	44	44
	FCNI3	20	7
	FCNI5	3	1
211A	FCNI1	2	10
	FCNI3	2	3
	FCNI5	2	1
219 A	FCNI1	1	3
	FCNI3	7	3
	FCNI5	5	1

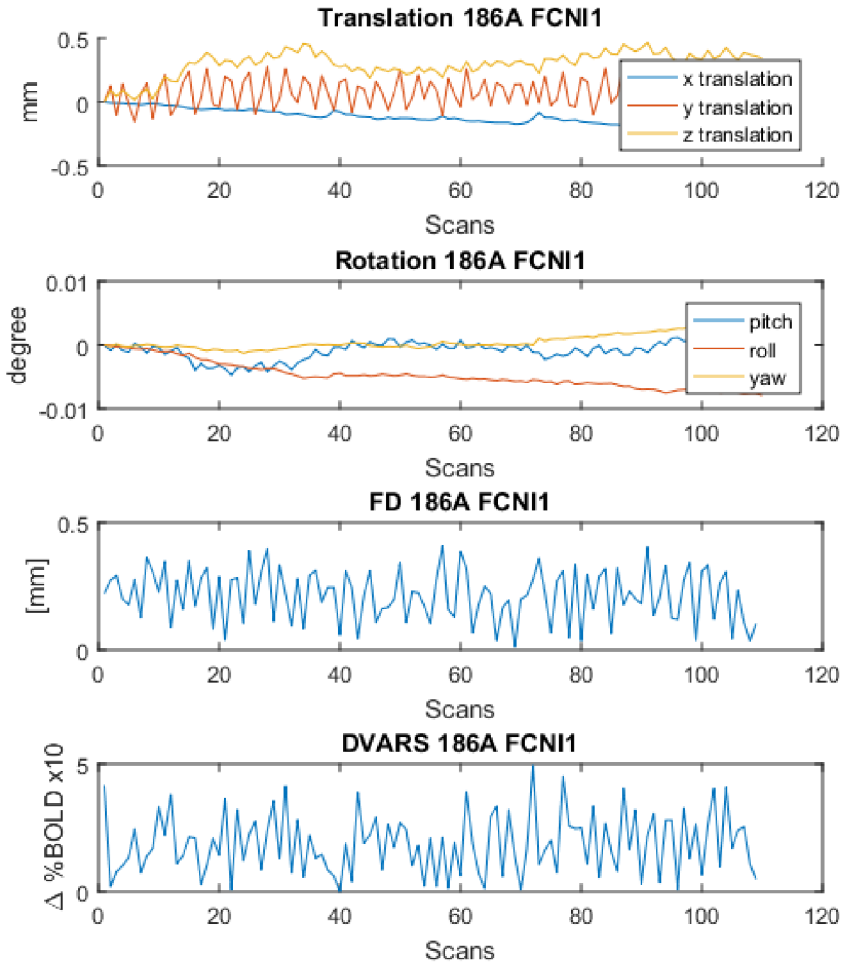

Fig. 10.2: Example of motion prevalence in 186A FCNI1

10.3 Overview of Analyzed Models

For each dataset presented in table 10.2, we constructed 9 analysis models, summarized in table 10.3. The first model having no motion-reducing features whatsoever, the second having the same parametres (i.e. 6 motion regressors) that are widely used in concurrent studies and the following models representing various combinations of the motion-reducing methods proposed formerly in this thesis.

Tab. 10.3: Nine Created Models for Subsequent Analyzes

Model	Motion Reg.	Spike Reg.	Motion Scrubbing	Motion metric
Nono	-	-	-	-
6mr	6	-	-	-
6FdSPIKE	6	0S-1S-0S	-	FD
6Fd3SPIKE	6	1S-1S-2S	-	FD
6FDvrSPIKE	6	0S-1S-0S	-	FD+DVARS
6LinFd	6	-	linear	FD
6LinFDvr	6	-	spline	FD
6SplFd	6	-	linear	FD+DVARS
6SplFDvr	6	-	spline	FD+DVARS

Table 10.4 illustrates the extent of motion in active periods for every chosen metric in this thesis.

Tab. 10.4: Motion Prevalence in Active Periods

Session	Metric	186A [%]	190A [%]	211A [%]	219A [%]
FCNI1	FD	0	34.0	1.9	0.1
	FD3	0	77.4	5.7	3.8
	FDvars	0	56.6	7.5	5.7
FCNI3	FD	0	21.2	2.8	3.4
	FD3	0	55.3	8.4	9.0
	FDvars	0	24.0	3.9	3.4
FCNI5	FD	0	1.7	1.4	0.6
	FD3	0	5.8	5.2	1.4
	FDvars	0	1.7	2	0.6

11 RESULTS

Figure 11.1 presents the mean T-statistics for session FCNI1 for all subjects. As one might expect, for the model totally free of motion (186A), the statistics did not change over the analyzed models; same as for 219A. There again, all the models yielded worse results than the untreated data (NoNo).

More interesting results came with subject 190A, which exhibited quite drastic motion prevalence (for some indicators almost 40 %, see 10.4). Model 6FD3Spike clearly reached the highest mean T-statistics, followed by the conventional 6-motion-parameters (6mr) method. Surprisingly, the lowest mean T-statistics were found in both models that use spline interpolations, 6SplFd and 6SplFDVr. 211A displays the same outcome, yet with smaller differences. This is quite logical, 211A had much less motion, therefore, the differences between the models does not stand out so much (again, check the motion prevalence in 10.4).

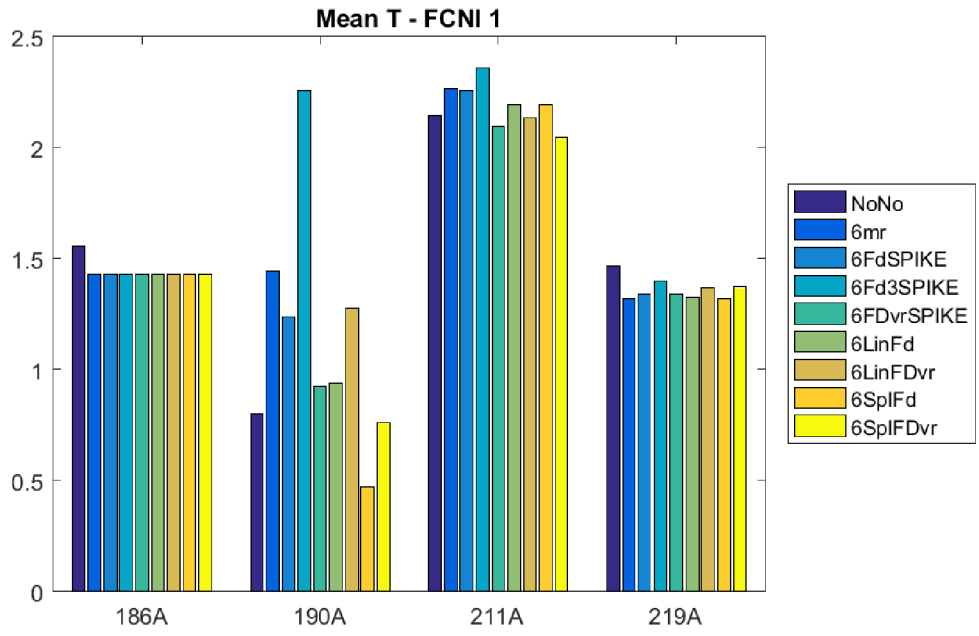

Fig. 11.1: Mean T-statistics for session FCNI1 across all subjects

The activation brain map of T-statistics for the conventional motion-treating model 6mr is depicted in figure 11.2. One can see how the number and intensity of expectantly active voxels in the occipital lobe (recall that the task was visual) is diminishing with the level of motion: from strong activations in 186A to relatively weak activations in 190A.

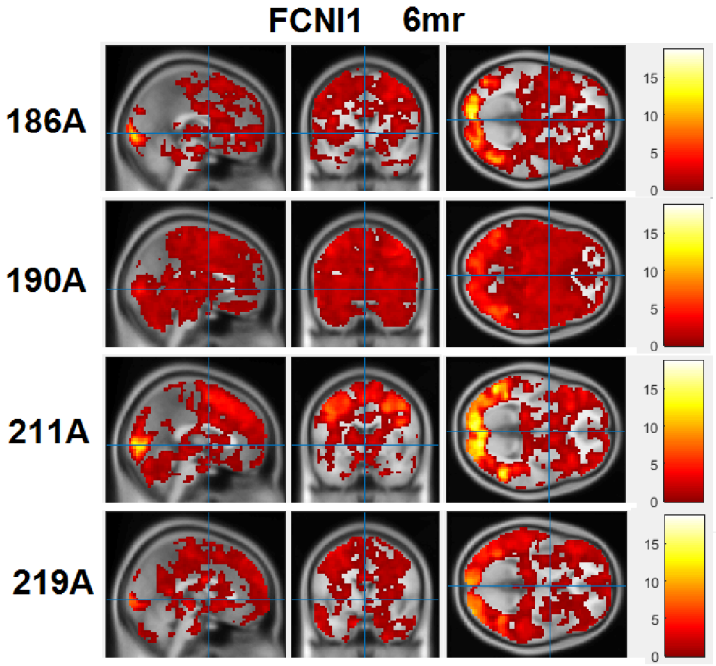

Fig. 11.2: Activation brain map for the model 6mr

Figure 11.3 shows the residual mean squared error (Res MS). In other words, the unexplained signal from GLM. The sheer negative effect of spline interpolations in 190A is obvious upon a brief look. This is also quite logical, there are simply not enough good adjacent timepoints that the interpolation could satisfyingly grasp.

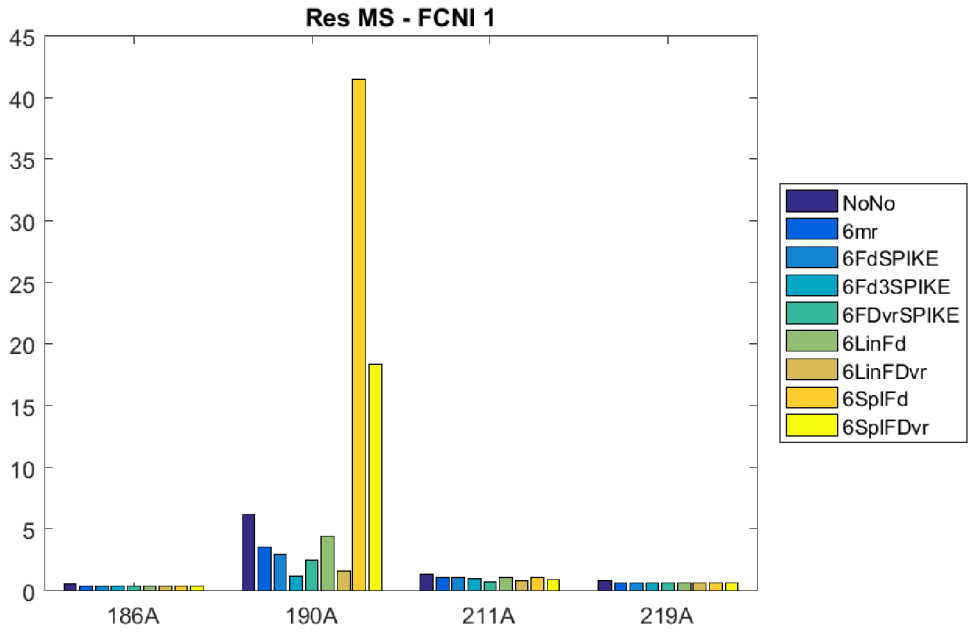

Fig. 11.3: Residual MS in FCNI1

The brain map of Res MS, depicted in 11.4, explores the effect even more. Whereas in the motion-untreated model, the highest value of Res MS is about 140 and the map has almost uniform values; maps of 6SplFD and 6SplFDVr are full of extremes, often going beyond the color scale. After a closer inspection of the data it turned out that the maximal values are around 5500 and 1500, respectively. Extremes like these consequently push up the overall average of Res MS to high values. On the other hand, however, in certain parts of the brain, for instance in some parts of the occipital lobe in model 6SplFD, Res MS was effectively reduced.

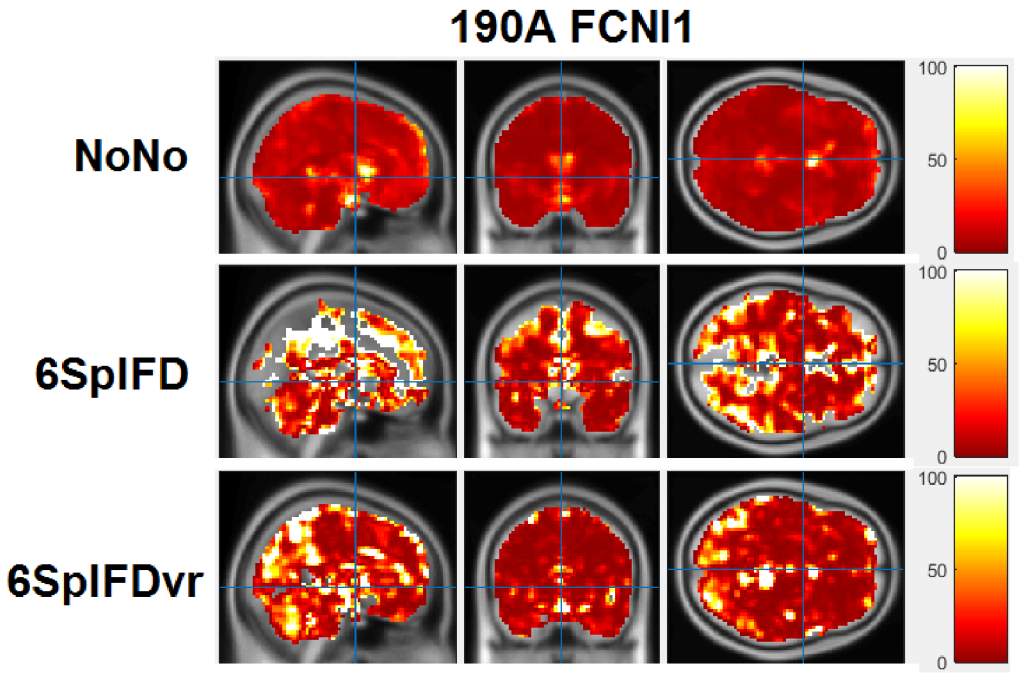

Fig. 11.4: Comparison of Res MS brain maps

Mean T-statistics and the residual mean squared error focus on the whole brain. Yet our goal is to look more deeply into the voxels whose activity correlated with the task, i.e. voxels with high T-statistics, the 'active' voxels. For this reason we constructed two new metrics: mean of 50 highest T-statistics (Mean T50) and the corresponding Res MS of those voxels (Res MS50).

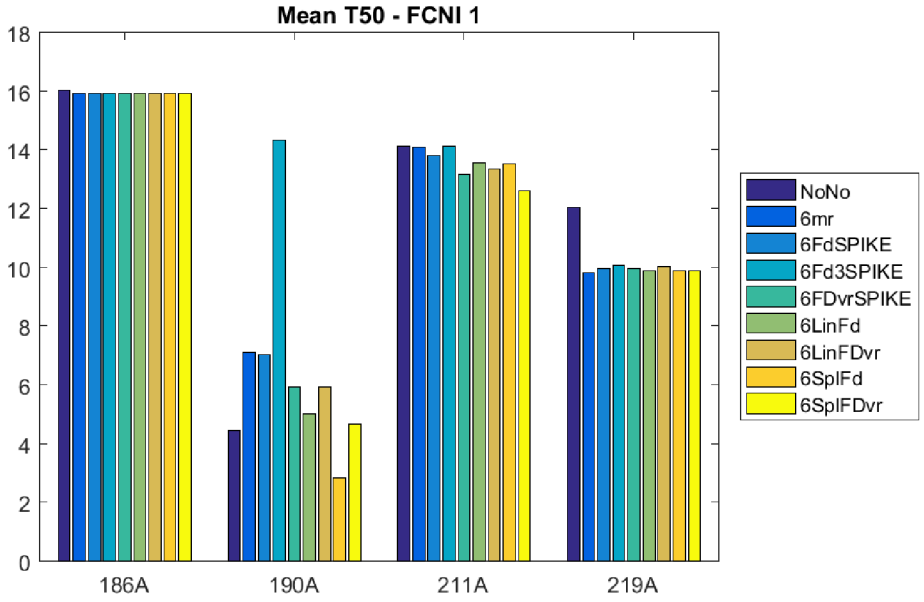

Fig. 11.5: Mean T50 for FCNI1 (T-statistics for 50 strongest voxels)

The outcomes of Mean T50 are more or less the replications of the outcomes of the regular mean T-statistics over the whole brain, with the difference that the effects of the individual modules are more emphasized here. Interestingly, all the motion-treating models had negative effects for the subject 219A. This could suggest that the motion artifacts were not localized in the voxels of the highest T-statistics.

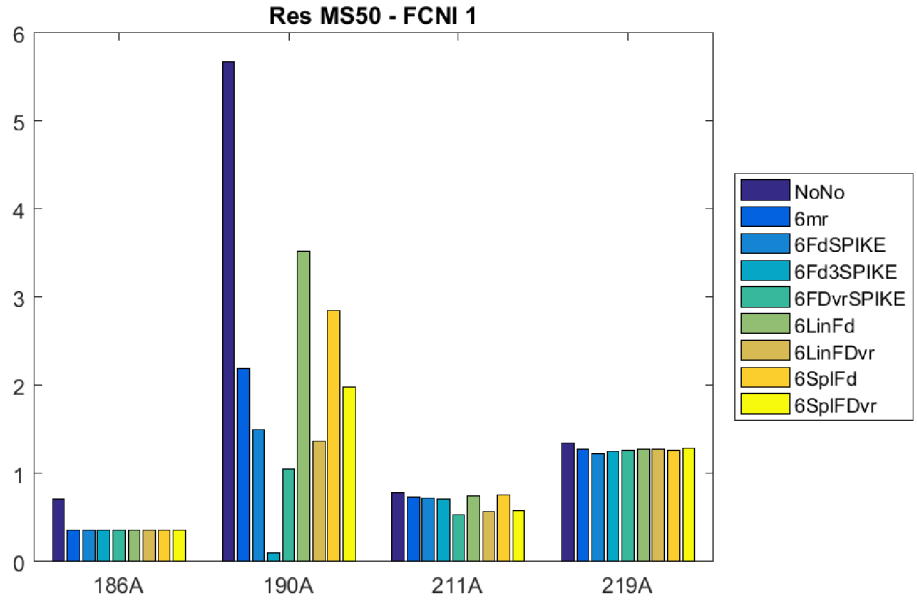

Fig. 11.6: Res MS50 for FCNI1

The residual mean squared error of the 50-T-strongest voxels in figure 11.6 allows one to change his or her perspective on the sheer negative effects of the spline interpolations. This new outlook suggests the splines did quite a good job for those highly active voxels: in terms of the residual mean squared error, both spline interpolations yielded better results than the motion-untreating model 6mr. It seems as if the splines could not satisfyingly interpolate the regular stochastic processes of inactive voxels. The causes of such unstable behavior of spline interpolations are elaborated on more fully in the Discussion section.
Again, one can see how well model 6Fd3SPIKE handled the reduction of motion by the little unexplained signal it left.

6Fd3SPIKE performs very well, however, the vast number of regressors comes with the cost of a decrease of the degree of freedom, which raises the analysis threshold, shown in figure 11.7.

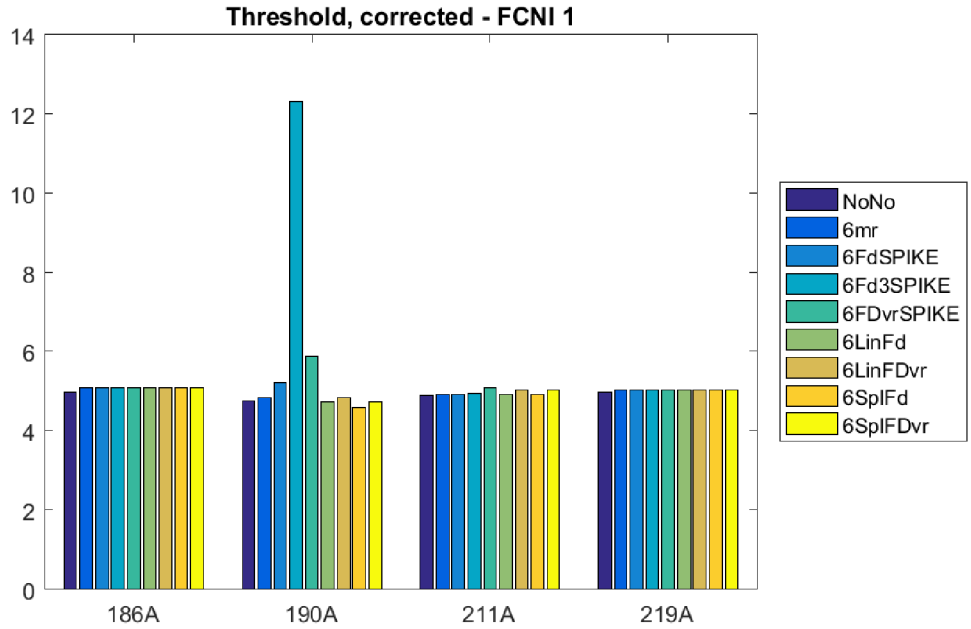

Fig. 11.7: T-statistics thresholds for FCNI1

The question is whether this high threshold would not eliminate all voxels. Upon looking at figure 11.8, one can see there are still some remaining. However, the impact of such drastic motion disturbance is embodied in the very few resulting voxels. In fact, for model 6SplFd there are no voxels that would pass the threshold at all.

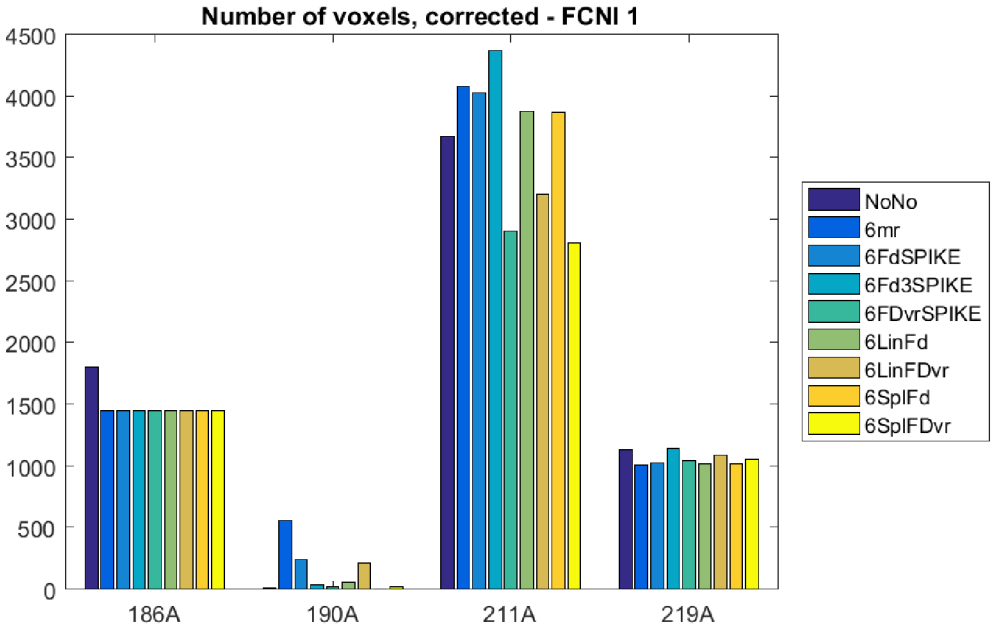

Fig. 11.8: Number of voxels that passed T-statistic thresholds

The activation brain map in figure 11.9 reveals that significant parts of the active voxels of model 6Fd3SPIKE are localized outside of the occipital lobe, suggesting that those activated voxels are actually falsely positive. According to this brain map, models 6mr and 6FdSPIKE provided much better results than one might have predicted from the previous charts.

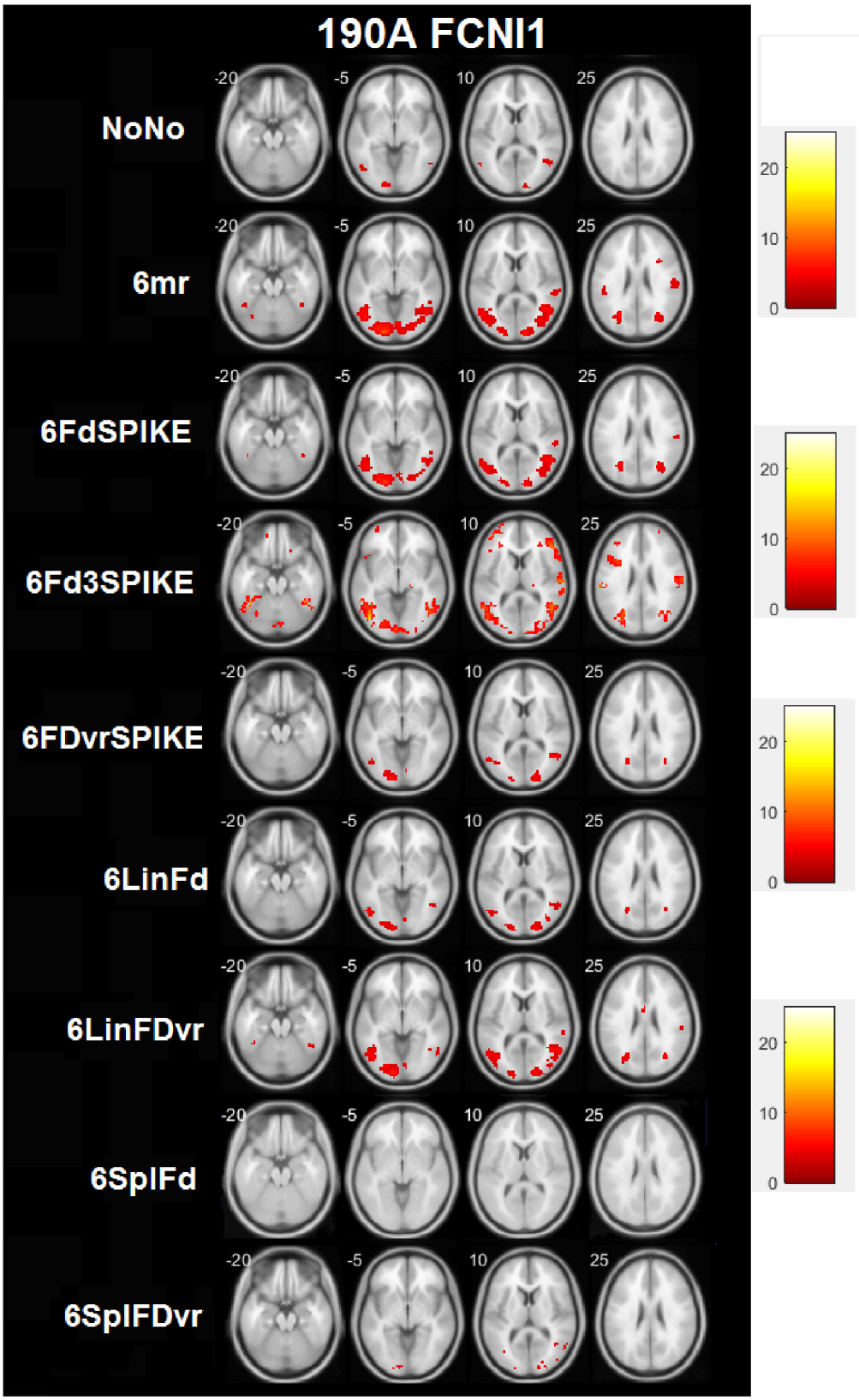

Fig. 11.9: Activation brain maps of all the models for 190A FCNI1

Our finding that model 6Fd3SPIKE does not perform as well as we once thought is only augmented after a closer inspection of the mean T-statistics for sessions FCNI3 (figure 11.10) and FCNI5 (figure 11.11). Moreover, according to figure 11.11, 6Fd3SPIKE yields one of the poorest results for both subjects 190A and 219A. The rest of the models seem to produce comparable outcomes with minor differences. In FCNI5 there are no radical deviations in the results across the models due to the small amount of motion that occurs in this session. The mean T50 charts, available in the supplementary materials, of both sessions provide almost similar outcomes.

Interestingly, the highest variability is caused by the interindividual variations of the subjects: note how much the T-statistics vary across subjects.

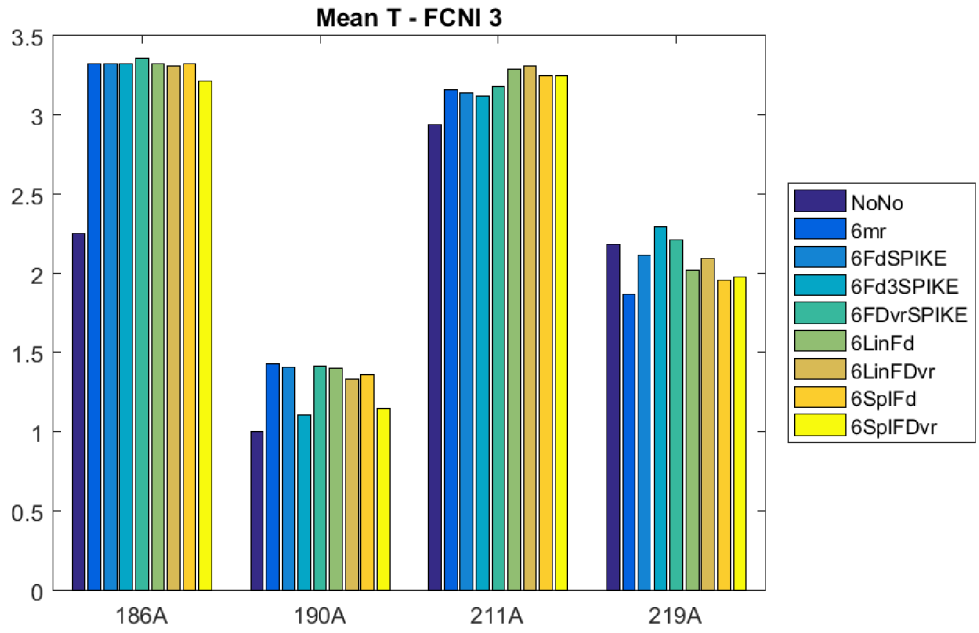

Fig. 11.10: Mean T-statistics for session FCNI3 across all subjects

The comparison of activation brain maps in figure D.3 reveals the discrepancy in the outcomes of 6Fd3SPIKE between session FCNI1 and session FCNI3. While in FCNI1 the model generated a variety of falsely positive voxels, in FCNI3 it produced plenty of falsely negative voxels.

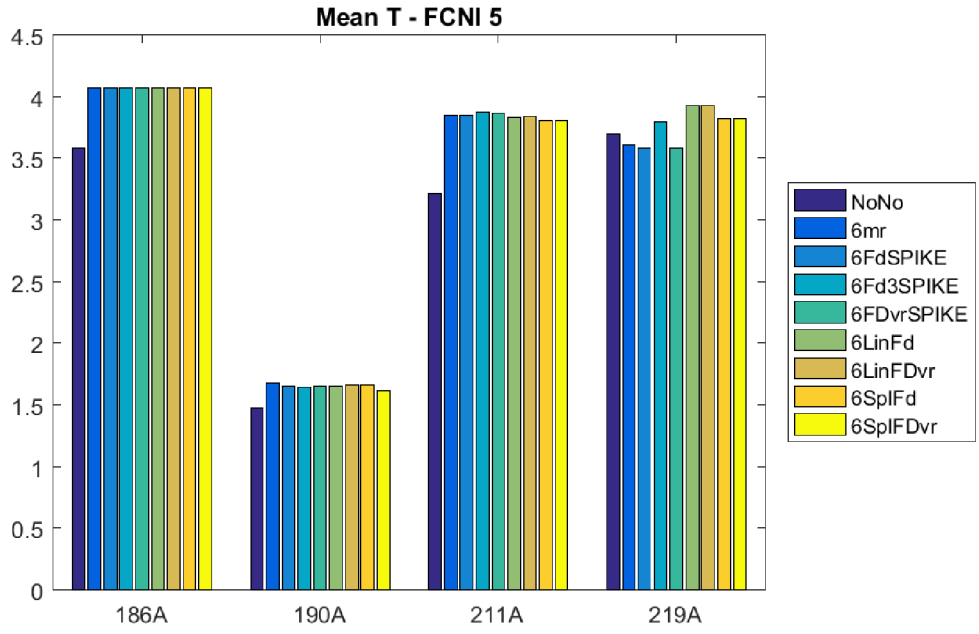

Fig. 11.11: Mean T-statistics for session FCNI5 across all subjects

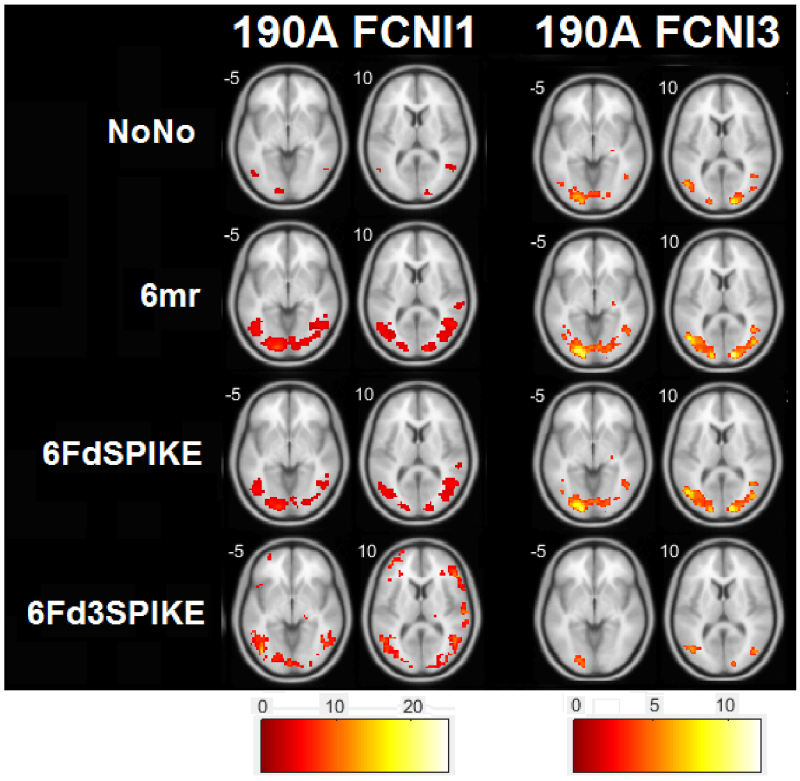

Fig. 11.12: Comparison of activation brain maps between session FCNI1 and FCNI3 for subject 190A

12 DISCUSSION

Of the models using the spike regression method, the model 6Fd3SPIKE, which first seemed like the ultimate model for reducing motion artifact, turned out to behave very unstably. In one case the model produced a great many of falsely positive results, in the other a great many of falsely negative results. It is hard to state whether this behavior could be attributed to the nature of the model or to the fact that either of the datasets is an outlier. We simply do not have enough data. The model 6FdSpike, that did not convincingly prove its strength in any of the statistics charts, however, seems to yield much better results than 6Fd3SPIKE when judged from the activation brain map in figure D.3. According to this figure, 6FdSpike did not produce any falsely positive nor falsely negative results. A similar model, 6FD-vrSPIKE, that uses a fused combination of motion indicators of FD with DVARS did not yield any improved outcomes compared to 6FdSpike.

Linear interpolations models, 6LinFD and 6LinFDvr, exhibited stable behavior across all datasets; however, none of their results turned out to be better than the conventional 6mr method. The same cannot be said about spline interpolation models. On the one hand, some of the results they produced were better than the results of the 6mr model; however, they behaved very unstably and unpredictably in every outcome of the analysis. It is conceivable that they could be used for data with a small amount of motion. Nonetheless, when the motion prevalence is high, they tend to produce unrealistic timecourses that are full of extreme values (see figure 11.3). This might be attributed to the great number of bad timepoints that are hard to fit when there are only a few good timepoints, the more when there is a cluster of bad timepoints. The interpolation then has to reach out for distant timepoints. Another reason why spline interpolations yielded such poor results might be that bad timepoints from active periods were interpolated, using good timepoints from passive periods and vice versa. As a result, it produced even worse signal timecourses than the original untreated data had.

From those results it is very difficult to suggest one ultimate method that would be best for reducing motion artifact. The study would have to have much more data to mitigate any interindividual variations of the subjects' brain connectivity. Thus, in conclusion, this thesis suggests to still use the conventional 6-motion-parameters method and recommends to do a much more robust study with the same models involved.

13 CONCLUSION

This bachelor thesis deals with the reduction of movement artifacts in BOLD fMRI data using rejection of motion-corrupted scans. In total nine different models designed for elimination of such scans were implemented in the MATLAB environment and evaluated on datasets provided by the Multimodal and Functional Imaging Laboratory of CEITEC MU.

The thesis is divided into 11 sections. The first section places fMRI in respect to other functional imaging techniques and briefly touches on the principles of PET, EEG and MEG. The second section explains the underlying phenomena of (f)MRI and image acquisition. The third section deals with generation of the BOLD fMRI signal and its properties. The fourth section describes several common artifacts and noises in the data. The fifth section outlines the preprocessing steps of BOLD fMRI data. The sixth section explains how the General Linear Model works and what role regressors play. The seventh section looks more deeply into the methods for locating motion-affected scans, while the eighth section explains methods for removing such scans. The ninth section introduces those methods more thoroughly and illustrates their outputs. The tenth section specifies chosen data and statistical models and illustrates the processing procedure in greater detail. The eleventh section presents the results and compares statistical models with each other. The twelfth section discusses the results and suggests suitable methods for removing motion artifact from BOLD fMRI data.

The supplementary materials contain figures specifying motion prevalence for each subject and session and detailed outcomes of statistical analyzes that were not presented in the text.

The results are ambiguous regarding indicating one best method that would conclusively stand out. For this reason, the thesis suggests to using conventional 6 motion parameters method until any more robust study concludes otherwise.

BIBLIOGRAPHY

[1] Basu, S.; Hess, S.; Braad, P.-E. N.; aj.: The basic principles of FDG-PET/CT imaging. *PET clinics*, rok 9, 4, 2014: s. 355–370, doi:10.1016/j.cpet.2014.07.006.
URL http://dx.doi.org/10.1016/j.cpet.2014.07.006

[2] Bright, M. G.; Murphy, K.: Is fMRI "noise" really noise? Resting state nuisance regressors remove variance with network structure. *NeuroImage*, rok 114, jul 2015: s. 158–169, doi:10.1016/j.neuroimage.2015.03.070.
URL https://doi.org/10.1016/j.neuroimage.2015.03.070

[3] Carp, J.: Optimizing the order of operations for movement scrubbing: Comment on Power et al. *Neuroimage*, rok 76, 2013: s. 436–438, doi:10.1016/j.neuroimage.2011.12.061.
URL https://doi.org/10.1016/j.neuroimage.2011.12.061

[4] Collura, T. F.: History and evolution of electroencephalographic instruments and techniques. *Journal of clinical neurophysiology*, rok 10, 4, 1993: s. 476–504.

[5] Friston, K. J.; Williams, S.; Howard, R.; aj.: Movement-related effects in fMRI time-series. *Magnetic resonance in medicine*, rok 35, 3, 1996: s. 346–355, doi:10.1002/mrm.1910350312.
URL http://dx.doi.org/10.1002/mrm.1910350312

[6] Higgins, D.: *MRI Signal Sources*. [online] Revise MRI, accessed 4/11/2017.
URL http://www.revisemri.com/questions/basicphysics/t2star

[7] Huettel, S. A.; Song, A. W.; McCarthy, G.: *Functional magnetic resonance imaging*, rok 1. Sinauer Associates Sunderland, 2004, ISBN 0471491101.

[8] Kleinnijenhuis, M.: *Imaging fibres in the brain*, rok 159. Michiel Kleinnijenhuis, 2014, ISBN 978-94-91027-99-4.

[9] Lemieux, L.; Salek-Haddadi, A.; Lund, T. E.; aj.: Modelling large motion events in fMRI studies of patients with epilepsy. *Magnetic resonance imaging*, rok 25, 6, 2007: s. 894–901, doi:10.1016/j.mri.2007.03.009.
URL http://dx.doi.org/10.1016/j.mri.2007.03.009

[10] Lipton, M.: *Introducing MRI*. [online] YouTube, Albert Einstein College of Medicine, accessed 24/10/2017.
URL https://www.youtube.com/playlist?list=PLPcImQzEnTpz-5TzxyyoYSbiAa9xdd89l

[11] Lystad, R. P.; Pollard, H.: Functional neuroimaging: a brief overview and feasibility for use in chiropractic research. *The Journal of the Canadian Chiropractic Association*, rok 53, 1, 2009: str. 59.

[12] Mikl, M.: *Funkční magnetická rezonance / fMRI Brno*. [online] Research group at Masaryk University Brno, accessed 24/10/2017.
URL `http://fmri.mchmi.com/main_index.php?strana=16`

[13] Nunez, P. L.; Srinivasan, R.: *Electric fields of the brain: the neurophysics of EEG*. Oxford University Press, USA, 2006, ISBN 9780195050387.

[14] Penny, W. D.; Friston, K. J.; Ashburner, J. T.; aj.: *Statistical parametric mapping: the analysis of functional brain images*. Academic press, 2011, ISBN 9780123725608.

[15] Power, J. D.; Barnes, K. A.; Snyder, A. Z.; aj.: Spurious but systematic correlations in functional connectivity MRI networks arise from subject motion. *NeuroImage*, rok 59, 3, feb 2012: s. 2142–2154, doi:10.1016/j.neuroimage.2011.10.018.
URL `https://doi.org/10.1016/j.neuroimage.2011.10.018`

[16] Power, J. D.; Mitra, A.; Laumann, T. O.; aj.: Methods to detect, characterize, and remove motion artifact in resting state fMRI. *Neuroimage*, rok 84, 2014: s. 320–341, doi:10.1016/j.neuroimage.2013.08.048.
URL `https://doi.org/10.1016/j.neuroimage.2013.08.048`

[17] Power, J. D.; Schlaggar, B. L.; Petersen, S. E.: Recent progress and outstanding issues in motion correction in resting state fMRI. *Neuroimage*, rok 105, 2015: s. 536–551, doi:10.1016/j.neuroimage.2014.10.044.
URL `https://doi.org/10.1016/j.neuroimage.2014.10.044`

[18] Satterthwaite, T. D.; Elliott, M. A.; Gerraty, R. T.; aj.: An improved framework for confound regression and filtering for control of motion artifact in the preprocessing of resting-state functional connectivity data. *Neuroimage*, rok 64, 2013: s. 240–256, doi:10.1016/j.neuroimage.2012.08.052.
URL `https://doi.org/10.1016/j.neuroimage.2012.08.052`

[19] Stansburyl, D.: *fMRI In Neuroscience: The Basics*. [online] The Clever Machine | Topics in Computational Neurosience Machine Learning, accessed 27/10/2017.
URL `https://theclevermachine.wordpress.com/2012/11/23/fmri-in-neuroscience-the-basics/`

[20] Van Dijk, K. R.; Sabuncu, M. R.; Buckner, R. L.: The influence of head motion on intrinsic functional connectivity MRI. *Neuroimage*, rok 59, 1, 2012: s. 431–438, doi:10.1016/j.neuroimage.2011.07.044.
URL `https://doi.org/10.1016/j.neuroimage.2011.07.044`

LIST OF SYMBOLS, PHYSICAL CONSTANTS AND ABBREVIATIONS

MR	Magnetic resonance
RF pulse	radiofrequency pulse
EEG	Electroencephalography
fMRI	Functional magnetic resonance imaging
MEG	Magnetoencephalography
PET	Positron-emission tomography
F-18	Fluorine-18
EPI	echoplanar imaging
GRE	gradient echo
FDG	Fluorodeoxyglucose
TR	repetition time
TE	echo time
HRF	hemodynamic response function
MNI	Montreal Neurological Institute
FWHM	full width at half maximum
GMS	grand mean scaling
GLM	general linear model
FD	framewise displacement
DVARS	framewise displacement
ICA	Independent Components Analysis
CompCor	Component Based Noise Correction Method
tfMRI	task-fMRI
ResMS	Residual mean squared error

LIST OF APPENDICES

A EXAMPLES OF SOURCE CODES

A.1 FD

One of the reasons why FD is so widely used is its easy implementation and computation. The code can be shrunk into a few lines:

Listing A.1: Code for FD Computation in the MATLAB Environment

```
B=importdata([path,'\',jmeno.name]); %parameters from RBt
B(:,4)=B(:,4).*(50*pi/180); %rot. conversion
B(:,5)=B(:,5).*(50*pi/180);
B(:,6)=B(:,6).*(50*pi/180);
FD=sum(abs(diff(B)),2)';
   for i= 1:length(FD)
      if(FD(i)>0.5)
        indexes=[indexes i];  %0.5 mm thresh.
      end
   end
```

A.2 DVARS

Unlike FD, DVARS uses data of the individual scans, not from a single matrix. The importation of the data is done via SPM12 functions. This makes the computation a bit longer.

Listing A.2: Code for DVARS Computation in the MATLAB Environment

```
filenames = spm_select('FPList',datadir,'^swu.*\.nii');
volumes = spm_vol(filenames); %import data
[Y] = spm_read_vols(volumes);
indexes=[];
%% Compute
 for i=1:(size(volumes,1)-1)
  dvars_sum(i)=sum(sum(sum(Y(:,:,:,i))));
  dvars_dif(i)=sum(sum(sum(Y(:,:,:,i+1)-Y(:,:,:,(i)))));
 end
 DVARS = 1000*sqrt((dvars_dif./dvars_sum).^2);
 for i= 1:length(DVARS)
  if(DVARS(i)>5)    %5 % threshold
    indexes=[indexes i];
  end
 end
```

B OVERVIEW OF MOTION PREVALENCE IN THE DATA

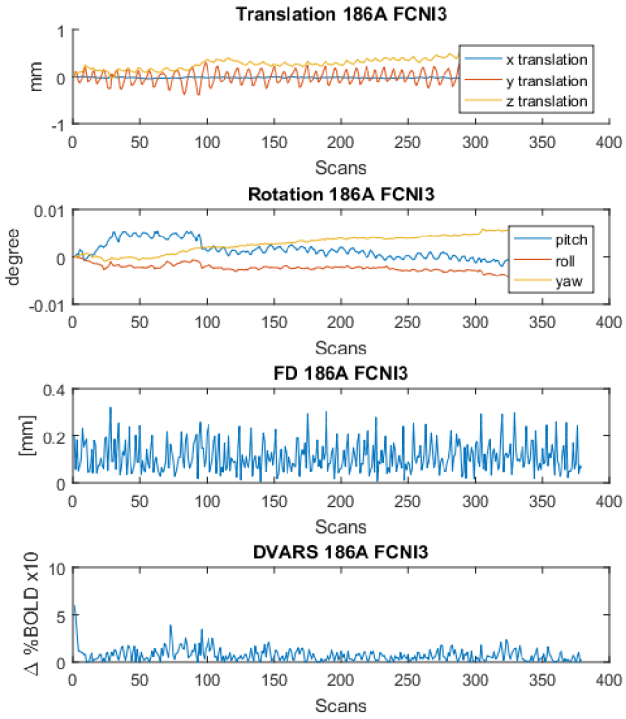

Fig. B.1: Motion prevalence in 186A FCNI3

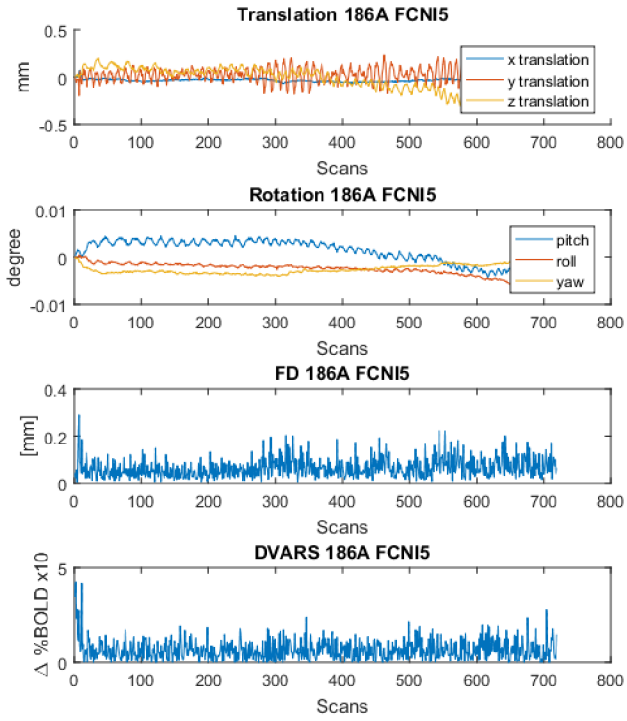

Fig. B.2: Motion prevalence in 186A FCNI5

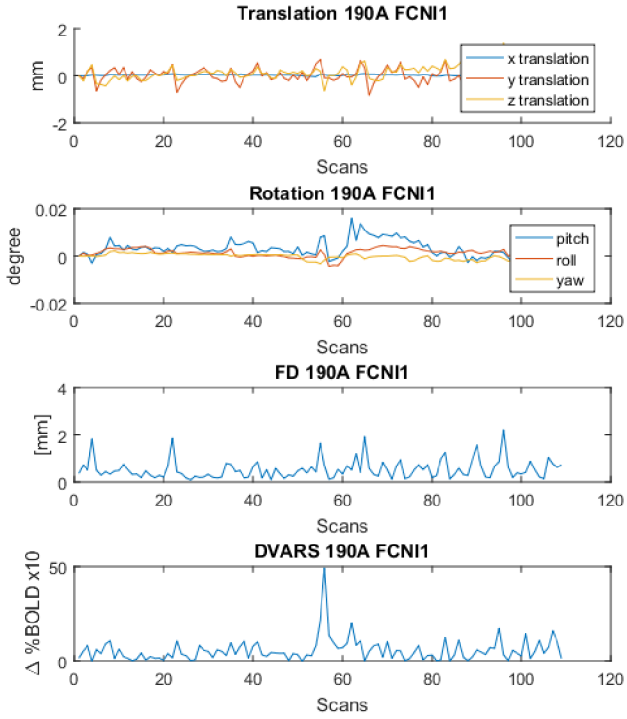

Fig. B.3: Motion prevalence in 190A FCNI1

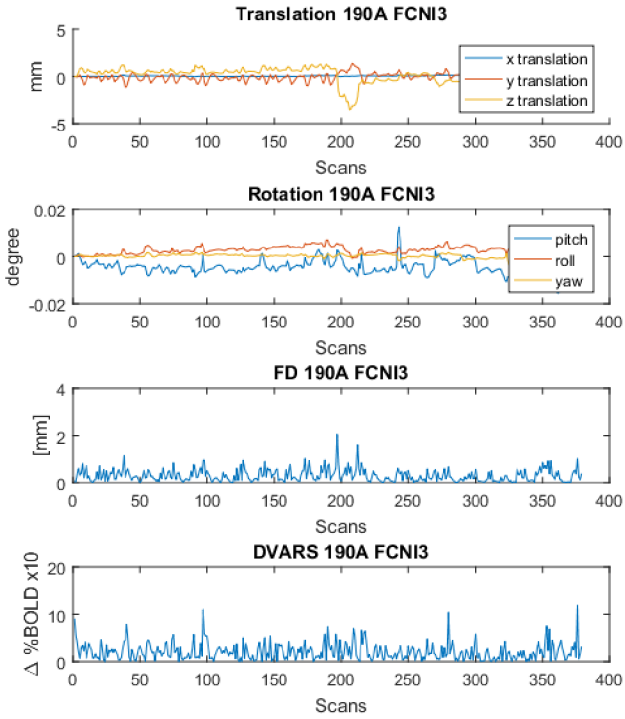

Fig. B.4: Motion prevalence in 190A FCNI3

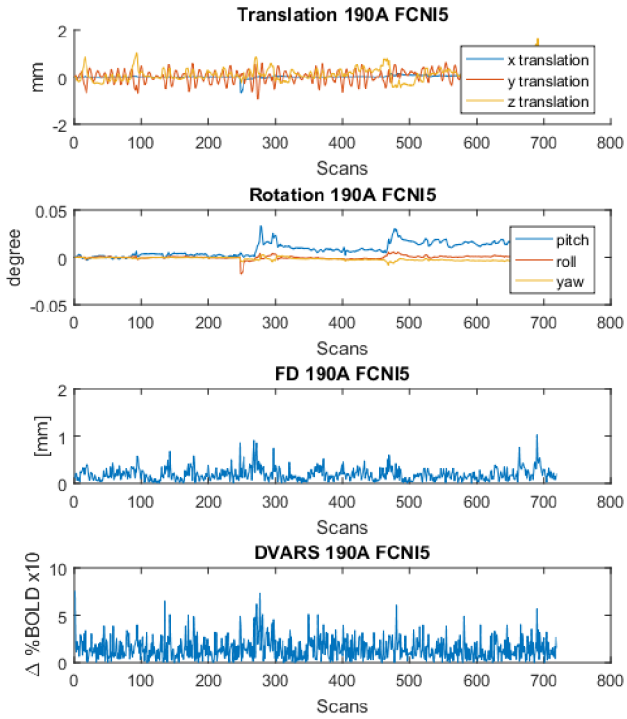

Fig. B.5: Motion prevalence in 190A FCNI5

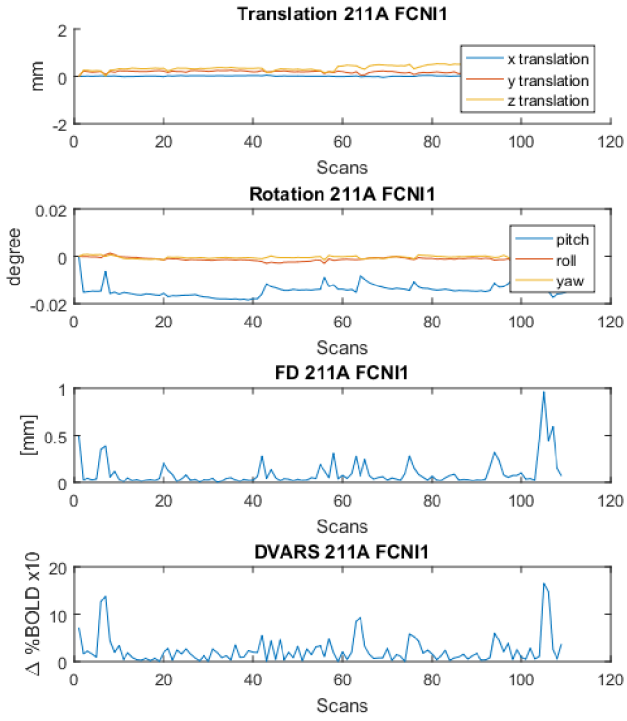

Fig. B.6: Motion prevalence in 211A FCNI1

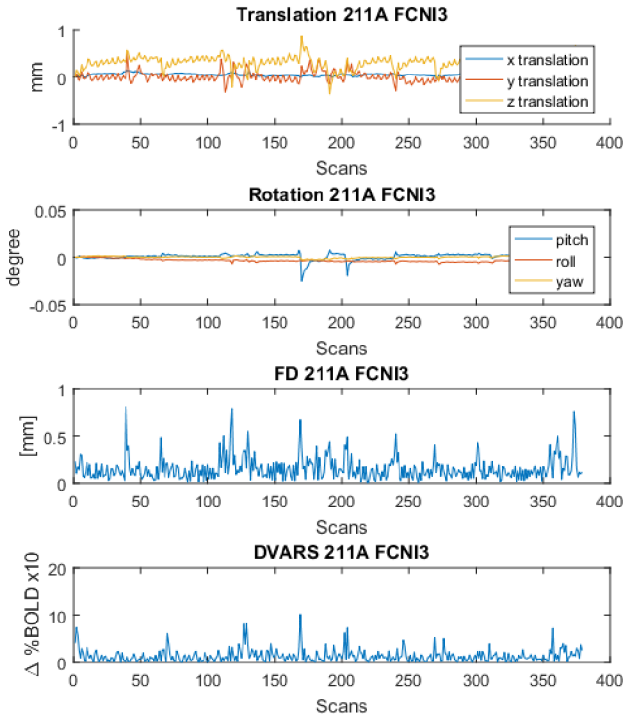

Fig. B.7: Motion prevalence in 211A FCNI3

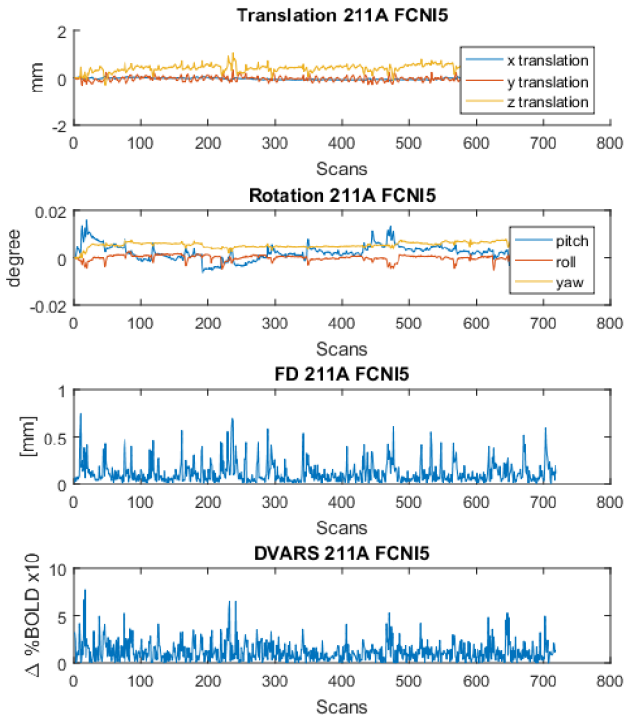

Fig. B.8: Motion prevalence in 211A FCNI5

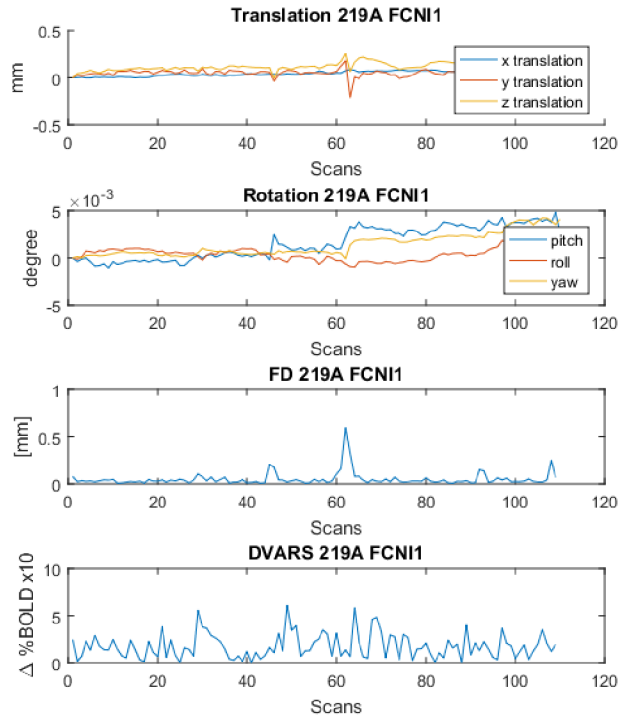

Fig. B.9: Motion prevalence in 219A FCNI1

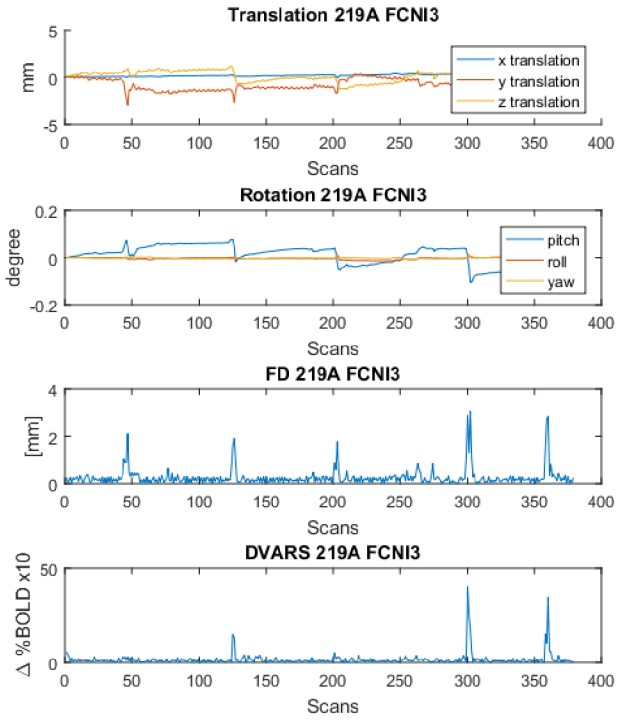

Fig. B.10: Motion prevalence in 219A FCNI3

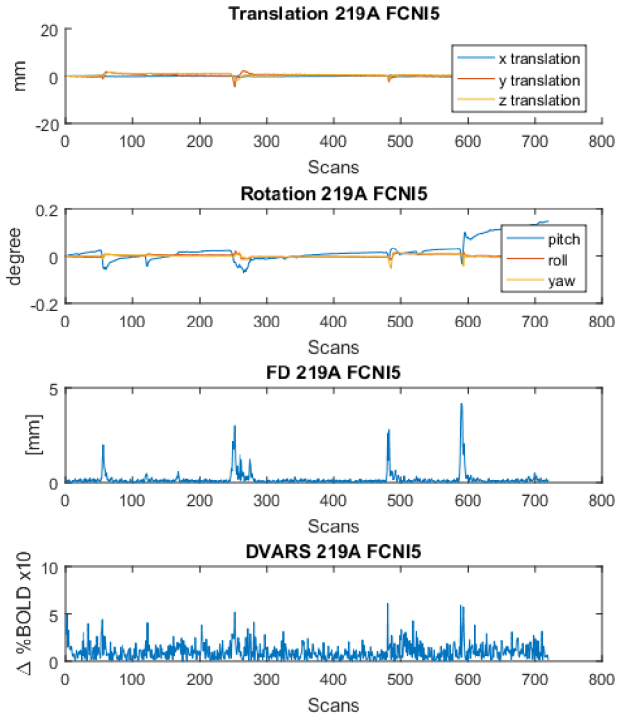

Fig. B.11: Motion prevalence in 219A FCNI5

C COMPUTATION TIMES OF LINEARLY INTERPOLATED SCANS

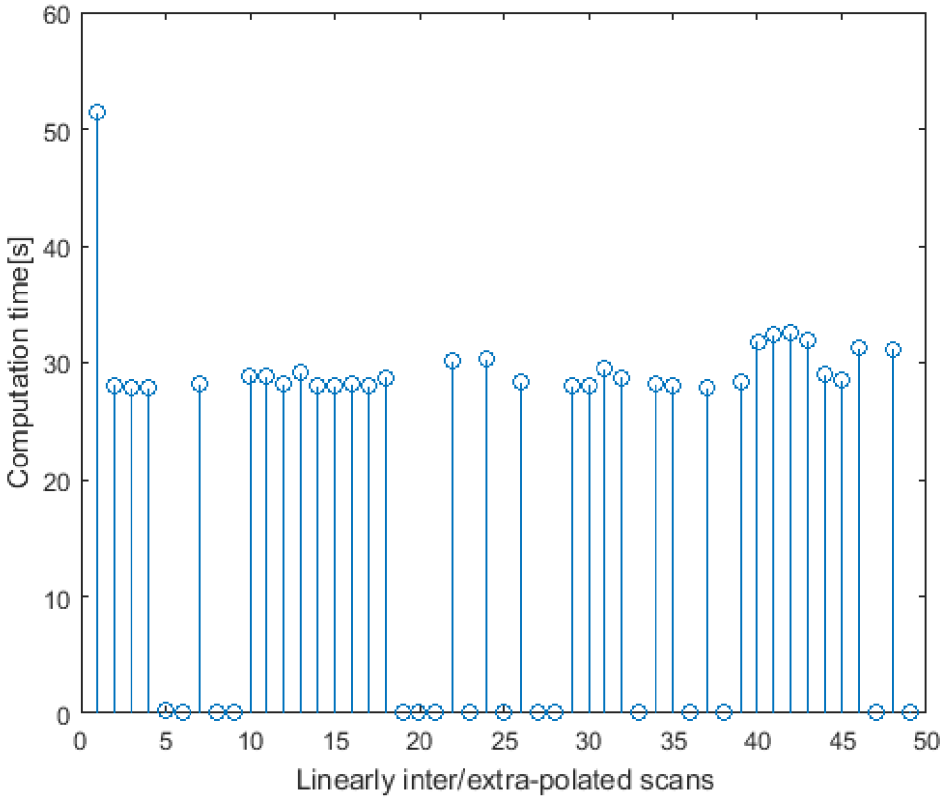

Fig. C.1: Computation times of linearly interpolated scans. Note that some scans were interpolated simply via MATLAB's direct matrix-wise operations, which took a minimum amount of time, others were interpolated timepoint by timepoint using interp1 function.

D ADDITIONAL CHARTS AND BRAIN MAPS

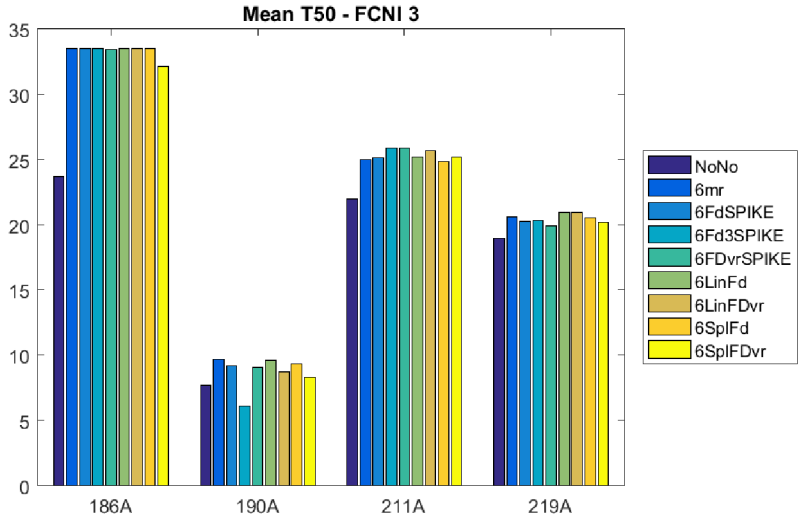

Fig. D.1: Mean T50 for FCNI3

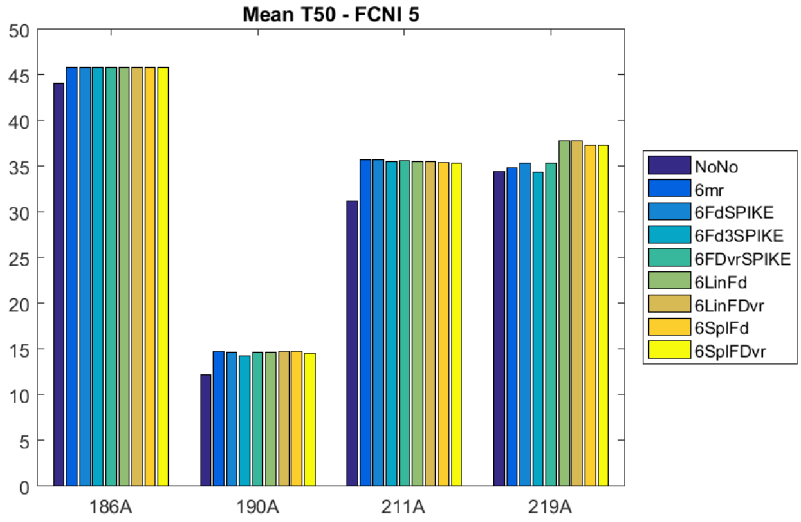

Fig. D.2: Mean T50 for FCNI5

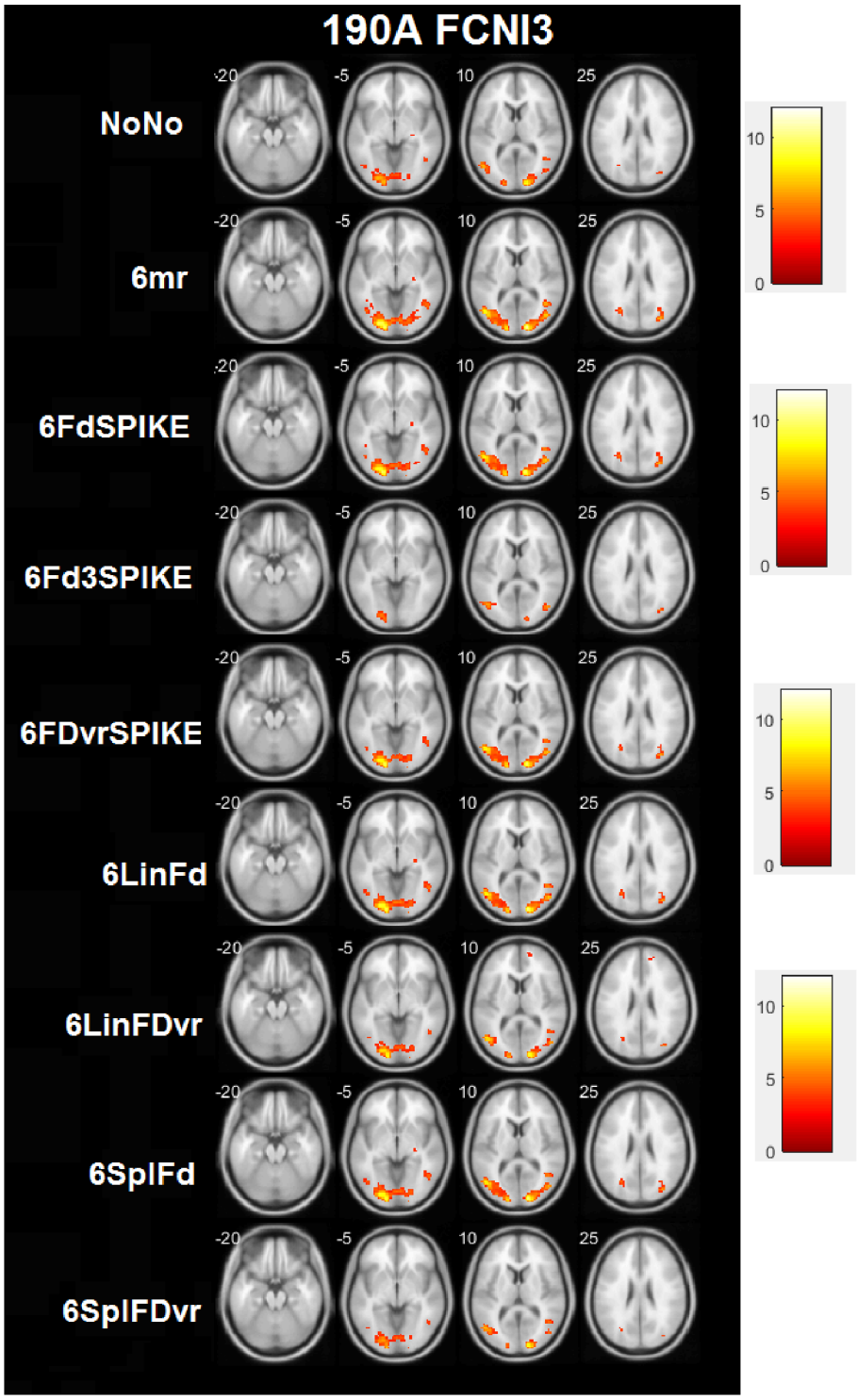

Fig. D.3: Activation brain maps of all models for 190A FCNI1

E CONTENTS OF THE ATTACHED CD

The attached CD contains the thesis, figures of the brain maps and statistical charts along with scripts, programmed in the MATLAB R2016a environment.

.3 SPM12_prep.m. . . . . The preprocessing of data, main body of the script. .3 SPM12_stat.m. . . . . A script that creates the statistical models, statistical evaluation.

```
/ . . . . . Directory tree of the attached CD
├── Thesis.pdf
└── Results
    ├── Brain maps. . . . . Activation brain maps, RES MS
    │   ├── 190AFCNI1pos.png
    │   ├── 190AFCNI3pos.png
    │   ├── FCNI1xFCNI3.png
    │   ├── P1NEWFCNI1map6mr.png
    │   ├── P1NEWFCNI3map6mr.png
    │   ├── P1NEWFCNI5map6mr.png
    │   ├── PNEWFCNI3map6mr.png
    │   └── SplResMSNoNo.png
    ├── Charts. . . . . Statistical charts
    │   ├── meanT1pos.png
    │   ├── meanT3pos.png
    │   ├── meanT5pos.png
    │   ├── meanT501.png
    │   ├── meanT503.png
    │   ├── meanT505.png
    │   ├── numvox_corrected1.png
    │   ├── numvox_corrected3.png
    │   ├── numvox_corrected5.png
    │   ├── numvox_uncorrected1.png
    │   ├── numvox_uncorrected2.png
    │   ├── numvox_uncorrected3.png
    │   ├── ResMS1.png
    │   ├── ResMS3.png
    │   ├── ResMS5.png
    │   ├── ResMS501.png
    │   ├── ResMS503.png
    │   ├── ResMS505.png
    │   ├── thr_corrected1.png
    │   ├── thr_corrected3.png
    │   └── thr_corrected5.png
    └── Motion prevalences. . . . . Motion prevalences, shown in the Appendix B
        ├── 186AFCNI1.png
        ├── 186AFCNI3.png
        ├── 186AFCNI5.png
        ├── 190AFCNI1.png
        └── 190AFCNI3.png
```

```
    ├── 190AFCNI5.png
    ├── 211AFCNI1.png
    ├── 211AFCNI3.png
    ├── 211AFCNI5.png
    ├── 219AFCNI1.png
    ├── 219AFCNI3.png
    └── 219AFCNI5.png
  ├── Flowchart.png ..... A flowchart of the data preprocessing
└── Scripts
  ├── AK_extract_ROIs.m. ..... A script that extracts statistical results
  ├── AK_results_.mat ..... The actual statistical results
  ├── dvars.m. ..... DVARS computation
  ├── FD_exe.m. ..... FD computation
  ├── FindFirstGood.m.. A function that finds a first good timepoint for the interp.
  ├── FindLastGood.m. .. A function that finds a last good timepoint for the interp.
  ├── Linear.m. ..... A function for the linear interpolation
  ├── MakeCharts.m. ..... A script for drawing charts
  └── Spline.m. ..... A function for the spline interpolation
```